The Astrophysical Journal, 935:157 (18pp), 2022 August 20 https://doi.org/10.3847/1538-4357/ac7fa0

Neutrino Emission from Luminous Fast Blue Optical Transients

Ersilia Guarini[1], Irene Tamborra[1], and Raffaella Margutti[2,3]
[1] Niels Bohr International Academy & DARK, Niels Bohr Institute, University of Copenhagen, Blegdamsvej 17, DK-2100, Copenhagen, Denmark
[2] Department of Astronomy, University of California, 501 Campbell Hall, Berkeley, CA 94720, USA
[3] Department of Physics, University of California, 366 Physics North MC 7300, Berkeley, CA 94720, USA
Received 2022 May 25; revised 2022 July 6; accepted 2022 July 6; published 2022 August 23

Abstract

Mounting evidence suggests that luminous fast blue optical transients (LFBOTs) are powered by a compact object, launching an asymmetric and fast outflow responsible for the radiation observed in the ultraviolet, optical, infrared, radio, and X-ray bands. Proposed scenarios aiming to explain the electromagnetic emission include an inflated cocoon, surrounding a jet choked in the extended stellar envelope. Alternatively, the observed radiation may arise from the disk formed by the delayed merger of a black hole with a Wolf–Rayet star. We explore the neutrino production in these scenarios, i.e., internal shocks in a choked jet and interaction between the outflow and the circumstellar medium (CSM). If observed on axis, the choked jet provides the dominant contribution to the neutrino fluence. Intriguingly, the IceCube upper limit on the neutrino emission inferred from the closest LFBOT, AT2018cow, excludes a region of the parameter space otherwise allowed by electromagnetic observations. After correcting for the Eddington bias on the observation of cosmic neutrinos, we conclude that the emission from an on-axis choked jet and CSM interaction is compatible with the detection of two track-like neutrino events observed by the IceCube Neutrino Observatory in coincidence with AT2018cow, and otherwise considered to be of atmospheric origin. While the neutrino emission from LFBOTs does not constitute the bulk of the diffuse background of neutrinos observed by IceCube, the detection prospects of nearby LFBOTs with IceCube and the upcoming IceCube-Gen2 are encouraging. Follow-up neutrino searches will be crucial for unraveling the mechanism powering this emergent transient class.

Unified Astronomy Thesaurus concepts: Particle astrophysics (96); Transient sources (1851); Neutrino astronomy (1100)

1. Introduction

The advent of time-domain astronomy has led to the discovery of intriguing new classes of transients that evolve on timescales $\lesssim$10 days (e.g., Poznanski et al. 2010; Inserra 2019; Modjaz et al. 2019; Drout et al. 2014; Arcavi et al. 2016). Among these, the fast blue optical transients (FBOTs; Drout et al. 2014; Arcavi et al. 2016; Tanaka et al. 2016; Pursiainen et al. 2018; Ho et al. 2021) exhibit unusual features. They have a rise time of a few days in the optical—$t_{\rm rise}$ up to 3 days, i.e., much faster than typical supernovae (SNe; e.g., Vallely et al. 2020; Arcavi et al. 2016; Ho et al. 2021)—and their spectrum remains blue and hot throughout the whole evolution.

We focus on the subclass of optically luminous FBOTs (hereafter denoted with LFBOTs), with an absolute peak magnitude $M_{\rm peak} < -20$ (Ho et al. 2020; Coppejans et al. 2020; Ho et al. 2021). LFBOTs have a rate in the local universe $\lesssim$300 Gpc^{-3} yr^{-1}, i.e., $\lesssim$0.4%–0.6% of core-collapse SNe (Ho et al. 2020; Coppejans et al. 2020; Ho et al. 2021). To date, radio emission has been detected for five FBOTs, all belonging to the LFBOTs category: CSS161010, AT2018cow, AT2018lug, AT2020xnd, and AT2020mrf. LFBOTs have been detected in the hard X-ray band as well, although not yet in gamma-rays (i.e., with energies >200 keV; Ho et al. 2019; Margutti et al. 2019; Coppejans et al. 2020; Ho et al. 2020; Yao et al. 2022; Bright et al. 2022).

The radio signal associated with LFBOTs is consistent with the synchrotron radiation in the self-absorption regime, arising from the forward shock developing when the ejecta interact with the circumstellar medium (CSM). Broad hydrogen (H) emission features have been observed in the spectra of some LFBOTs, i.e., AT2018cow (Margutti et al. 2019; Perley et al. 2019) and CSS161010 (Coppejans et al. 2020). Moreover, the combined observations in the optical and radio bands suggest that the fastest component of the outflow is moving with speed $0.1c \lesssim v_{\rm f} \lesssim 0.6c$ (Perley et al. 2019; Ho et al. 2019; Margutti et al. 2019; Yao et al. 2022; Bright et al. 2022).

As for X-rays, the spectrum exhibits a temporal evolution and a high variability that is challenging to explain by invoking external shock interaction. Rather, the X-ray emission might be powered by a rapidly evolving compact object (CO), like a magnetar or a black hole, or a deeply embedded shock (Ho et al. 2019; Margutti et al. 2019). In addition, the interaction with the CSM cannot simultaneously explain the ultraviolet, optical, and infrared spectral features, e.g., the rapid rise of the lightcurve and its luminosity ($L_{\rm opt} \simeq 10^{44}$ erg s^{-1}), as well as the receding photosphere observed for AT2018cow at late times (Perley et al. 2019) and typically associated with an increase of the effective temperature. In the light of this growing set of puzzling data, multiple sites might be at the origin of the observed electromagnetic emission across different wave bands, together with an asymmetric outflow embedding the CO (Margutti et al. 2019). An additional piece of evidence of the presence of a CO might be the persistent ultraviolet source observed at the location of AT2018cow (Sun et al. 2022). The presence of a CO may also be supported by

the observation in AT2018cow of high-amplitude quasiperiodic oscillations in soft X-rays (Pasham et al. 2022).

Several interpretations of LFBOT observations have been proposed, such as shock interaction of an outflow with dense CSM (e.g., Fox & Smith 2019; Pellegrino et al. 2022; Leung et al. 2020; Xiang et al. 2021[4]); reprocessing of X-rays emitted from a central engine within a polar outflow (e.g., Margutti et al. 2019; Chen & Shen 2022; Calderón et al. 2021; Piro & Lu 2020; Uno & Maeda 2020; Liu et al. 2018; Perley et al. 2019; Kuin et al. 2019); a neutron star engulfed in the extended envelope of a massive red supergiant, leading to the common envelope evolution and formation of a jetted SN (Soker et al. 2019) or a related impostor (Soker 2022); the emission from the accretion disk originating from the collapse of a massive star into a black hole (Kashiyama & Quataert 2015; Quataert et al. 2019) or from the electron-capture collapse to a neutron star following the merger of a ONeMg white dwarf with another white dwarf (Lyutikov & Toonen 2019; Lyutikov 2022). Each of the aforementioned scenarios may only reproduce some of the observed features of LFBOTs.

Recently, two models have been proposed in the attempt of explaining the multiwavelength emission of AT2018cow. Gottlieb et al. (2022b) invoke the collapse of a massive star, possibly not completely H-stripped, which launches a jet. The jet may be off axis or choked in the extended stellar envelope and, therefore, not directly visible; to date, the direct associations between jets and LFBOTs are lacking, and constraints have been set for AT2018cow (Bietenholz et al. 2020). The jet interacts with the stellar envelope, inflating the cocoon surrounding the jet; the cocoon expands, breaks out of the star and cools, emitting in the ultraviolet, optical, and infrared. Metzger (2022) considers a delayed Wolf–Rayet star–black hole merger following a failed common envelope phase. This leads to the formation of an asymmetric CSM, dense in the equatorial region, and less dense in the polar one. The scenarios proposed by Gottlieb et al. (2022b) and Metzger (2022) successfully fit the ultraviolet, optical and infrared spectra of AT2018cow; Metzger (2022) also provides a fit to the X-ray data of AT2018cow. However, it is yet to be quantitatively proven that the off-axis jet scenario of Gottlieb et al. (2022b) is consistent with radio observations; no fit to the radio data is provided in Metzger (2022). It is unclear whether these models could explain the late time hot and luminous ultraviolet emission ($L_{\rm UV} \gtrsim 2.7 \times 10^{34}$ erg s^{-1}) detected in the proximity of AT2018cow (Sun et al. 2022). Metzger (2022) provides a possible explanation to this persistent emission as the late time radiation from the accretion disk surrounding the black hole resulting from the Wolf–Rayet star–black hole merger. Further observations in the direction of AT2018cow will eventually confirm this conjecture.

In order to unravel the nature of the engine powering LFBOTs, a multimessenger approach may provide a fresh perspective. In particular, the neutrino signal could carry signatures of the mechanisms powering LFBOTs. Since the first detection of high-energy neutrinos of astrophysical origin by the IceCube Neutrino Observatory, the follow-up searches are ongoing to pinpoint the electromagnetic counterparts associated to the IceCube neutrino events (Abbasi et al. 2021a; Garrappa et al. 2019; Acciari et al. 2021; Necker et al. 2022; Stein et al. 2022). A dozen of the neutrino events have been associated in likely coincidence with blazars, tidal disruption events, or superluminous SNe (Aartsen et al. 2018a; Giommi et al. 2020; Franckowiak et al. 2020; Garrappa et al. 2019; Krauß et al. 2018; Kadler et al. 2016; Stein et al. 2021; Reusch et al. 2022; Pitik et al. 2022). As for LFBOTs, the IceCube Neutrino Observatory reported the detection of two track-like muon neutrino events in spatial coincidence with AT2018cow in the 3.5 days following the optical detection. These neutrino events could be statistically compatible with the expected number of atmospheric neutrinos–0.17 events (Blaufuss 2018).

As the number of LFBOTs detected electromagnetically increases, the related neutrino emission remains poorly explored. Fang et al. (2019) pointed out that, if AT2018cow is powered by a magnetar, the particles accelerated in the magnetar wind may escape the ejecta at ultrahigh energies. Within the models proposed in Gottlieb et al. (2022b); Metzger (2022), additional sites should be taken into account for what concerns neutrino production. For example, if a choked jet powered by the central CO is harbored within the LFBOT (Gottlieb et al. 2022b), we would not observe any prompt gamma-ray signal. Nevertheless, efficient proton acceleration could take place leading to the production of TeV–PeV neutrinos (Murase & Ioka 2013; He et al. 2018; Meszaros & Waxman 2001; Razzaque et al. 2004; Ando & Beacom 2005; Nakar 2015; Senno et al. 2016; Xiao & Dai 2014; Fasano et al. 2021; Tamborra & Ando 2016; Denton & Tamborra 2018). In addition, Gottlieb et al. (2022b); Metzger (2022) predict fast ejecta propagating in the CSM with velocity $v_{\rm f} \gtrsim 0.1c$. Protons may be accelerated at the shocks between the ejecta and the CSM leading to neutrino production, similar to what is foreseen for SNe (Murase et al. 2011; Pitik et al. 2022; Petropoulou et al. 2017, 2016; Katz et al. 2011; Murase et al. 2014; Cardillo et al. 2015; Zirakashvili & Ptuskin 2016; Murase et al. 2020; Sarmah et al. 2022) or transrelativistic SNe (Kashiyama et al. 2013; Zhang & Murase 2019), probably powered by a choked jet as it may be the case for LFBOTs. Neutrinos produced from LFBOTs could be detectable by the IceCube Neutrino Observatory and the upcoming IceCube-Gen2, aiding to pin down the mechanisms powering LFBOTs (Murase & Bartos 2019; Fang et al. 2020).

Our work is organized as follows. In Section 2, we discuss the most promising particle acceleration sites for the models proposed in Gottlieb et al. (2022b) and Metzger (2022; a choked jet and/or a fast outflow emitted by the CO that propagates outwards in the CSM). Section 3 summarizes the model parameters inferred for AT2018cow and CSS161010 from electromagnetic observations. Section 4 focuses on the production of high-energy neutrinos. In Section 5, we present our findings for the neutrino signal expected at Earth from AT2018cow and CSS161010 and discuss the corresponding detection prospects. The contribution of LFBOTs to the neutrino diffuse background is presented in Section 6. Finally, we conclude in Section 7. The most relevant proton and meson cooling times are outlined in the Appendix.

2. Particle Acceleration Sites

In this section, we outline the mechanisms proposed in Gottlieb et al. (2022b; hereafter named "cocoon model") and Metzger (2022; hereafter "merger model") for powering LFBOTs that could also host sites of particle acceleration. First, we consider a jet launched by the central engine and choked in the extended stellar envelope. Then, we focus on the interaction between the fast ejecta and the CSM.

[4] We note, however, that the broadband X-ray spectrum of AT2018cow is unlike the thermal spectra of interacting SNe, and shows instead clear nonthermal features.

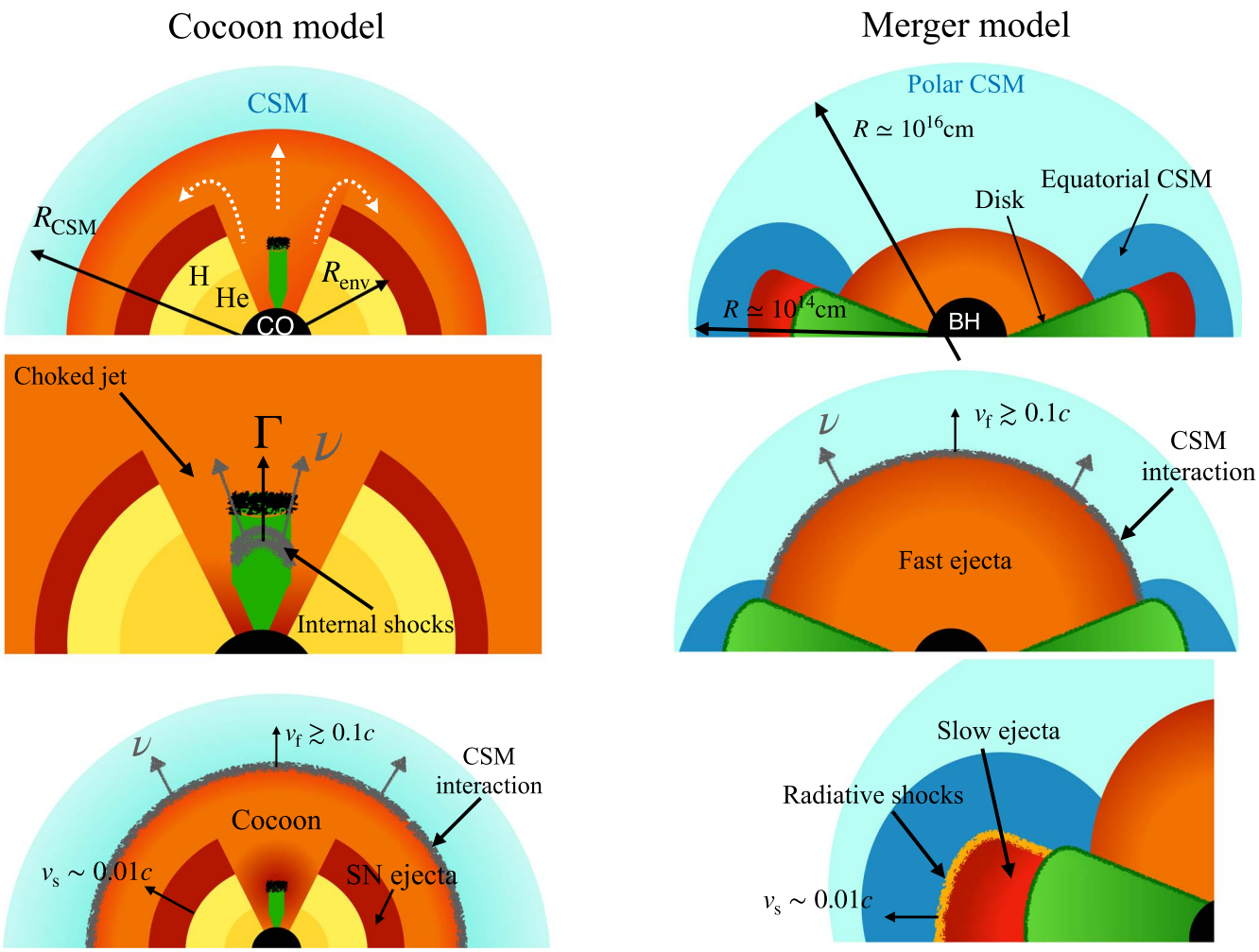

Figure 1. Cartoons of the cocoon model (left panels; Gottlieb et al. 2022b) and merger model (right panels; Metzger 2022), not to scale. For the sake of simplicity, we show only the upper half section of the FBOT. Top left panel: a massive star collapses, forming a CO (black region). The CO is surrounded by helium (He) and H envelopes (regions with yellow hues). The progenitor core ($R_\star \sim 10^{11}$ cm) is surrounded by an extended envelope (of radius R_{env}). Middle left panel: the jet (green) is launched near the surface of the CO, and it is choked in the extended envelope. Internal shocks occur in the proximity of the jet head (gray), where neutrinos can be produced. Bottom left panel: the jet inflates the cocoon (orange region); the latter breaks out from the stellar surface and interacts with the CSM (aqua outer region). The fastest component of the cocoon moves with $v_f \gtrsim 0.1c$, while its slow component (red region; SN ejecta) propagates with $v_s \simeq 0.01c$ in the equatorial direction. While the fast component of the cocoon propagates into the CSM, collisionless shocks take place (gray line surrounding the cocoon); here, neutrinos may be produced. Even though the geometry of the cocoon is not perfectly spherical, we assume spherical symmetry for the sake of simplicity in the analytical treatment of the problem; see main text. Top right panel: as a result of the Wolf–Rayet star–black hole merger, a black hole forms (BH; black), surrounded by an accretion disk (green region). The equatorial dense CSM (blue region) extends up to $\simeq 10^{14}$ cm, while the polar (aqua region) CSM extends up to $\simeq 10^{16}$ cm. Middle right panel: the disk emits a fast outflow (orange region) propagating in the polar direction with $v_f \simeq 0.1c$ into the CSM. Here, collisionless shocks (gray line) occur and neutrino production takes place. Bottom right panel: the slow outflow (red shell) is emitted from the disk in the equatorial direction, and it propagates with $v_s \simeq 0.01c$ into the dense equatorial CSM. Here, radiative shocks take place (orange line) and neutrino production is negligible with respect to the one from the polar outflow.

2.1. Choked Jet

Gottlieb et al. (2022b) propose that LFBOTs arise from the collapse of massive stars that result in the formation of a central CO, possibly harboring a relativistic jet, as shown in the left panels of Figure 1. If the jet were to successfully drill through the stellar envelope, it would break out and give rise to a gamma-ray bright signal. Nevertheless, no prompt emission has been detected in association with LFBOTs, suggesting that a successful jet could be disfavored (Margutti et al. 2019; Coppejans et al. 2020). The nondetection of gamma-rays hints that an extended envelope, probably not fully H-depleted in order to explain the broad emission features observed in some LFBOT spectra [AT2018co; Perley et al. 2019; Margutti et al. 2019; and CSS161010; Coppejans et al. 2020], may engulf the stellar core, extending up to $R_\star \simeq 10^{11}$ cm (Gottlieb et al. 2022b). In this case, the jet could be choked, as displayed in the middle left panel of Figure 1.

We consider a collapsing star that has not lost its H envelope completely, and it is surrounded by an extended shell of radius $R_{env} \simeq 3 \times 10^{13}$ cm and mass $M_{env} \simeq 10^{-2} M_\odot$ (Senno et al. 2016). The modeling of the extended H envelope mass is inspired by partially stripped SNe (e.g., Gilkis & Arcavi 2022; Nakar 2015; Sobacchi et al. 2017). We fix the value of M_{env} to avoid dealing with several free parameters (see Section 3) and leave to future work the assessment of the dependence of the neutrino signal on the mass of the extended envelope. For the extended envelope, we consider the following density profile (Nakar 2015):

$$\rho_{env}(R) = \rho_{env,0}\left(\frac{R}{R_{env}}\right)^{-2}, \quad (1)$$

where $\rho_{\rm env,0} = M_{\rm env}\left[\int^{R_{\rm env}} dR 4\pi R^2 \rho_{\rm env}(R)\right]^{-1}$, and R is the distance from the CO. We assume a fixed density profile for the extended envelope due to the lack of knowledge on its features; further investigations on the impact of this assumption on the neutrino signal is left to future work. Nevertheless, we expect that neutrino telescopes will not be sensitive to this dependence; see, e.g., Xiao & Dai (2014). The jet is launched near the surface of the CO,[5] with luminosity $\tilde{L}_j$, narrow opening angle θ_j.

For fixed θ_j, the dynamics of the jet only depend on the isotropic equivalent quantities. Hence, it is convenient to define the isotropic equivalent luminosity of the jet: $\tilde{L}_j^{\rm iso} = \tilde{L}_j/(\theta_j^2/4)$. Note that the isotropic equivalent quantities are always defined in the CO frame; for the sake of clarity, we keep the twiddle notation throughout the paper.

While the jet pierces through the stellar envelope, two shocks develop: a reverse shock (RS; Table 1), propagating back to the core of the jet, and a forward shock, propagating into the external envelope. The region between the two shocks constitutes the jet head. Denoting with Γ the Lorentz factor of the unshocked jet plasma (i.e., the bulk Lorentz factor of the jet) and with Γ_h the one of the jet head, the relative Lorentz factor is the following (He et al. 2018):

$$\Gamma_{\rm rel} = \Gamma\Gamma_h(1 - \beta\beta_h), \tag{2}$$

where $\beta = \sqrt{1 - 1/\Gamma^2}$, and $\beta_h = \sqrt{1 - 1/\Gamma_h^2}$. For a nonrelativistic jet head: $\Gamma_h \simeq 1$, which implies $\Gamma_{\rm rel} \simeq \Gamma$; this assumption is valid for the region of the parameter space of interest, as discussed in Section 3.

From the shock jump conditions, the energy densities in the shocked envelope region and in the shocked jet plasma at the position of the jet head $\tilde{R}_h \equiv R_h$, respectively, are as follows (Blandford & McKee 1976; Sari & Piran 1995):

$$e_{\rm sh,env} = (4\Gamma_h + 3)(\Gamma_h - 1)\rho_{\rm env}(R_h)c^2, \tag{3}$$

$$e_{\rm sh,j} = (4\Gamma_{\rm rel} + 3)(\Gamma_{\rm rel} - 1)n_j'(R_h)m_p c^2. \tag{4}$$

Here $n_j' = \tilde{L}_j^{\rm iso}/(4\pi R^2 m_p c^3 \Gamma^2)$ is the comoving particle density of the unshocked jet. Equating $e_{\rm sh,ext} = e_{\rm sh,j}$ and expanding around Γ_h for the nonrelativistic case, we obtain the speed of the jet head:

$$v_h \simeq \left[\frac{\tilde{L}_j^{\rm iso}}{(4\Gamma_h + 3)\pi c \rho_{\rm env}(R_h)R_h^2}\right]^{1/2}. \tag{5}$$

Since the jet head is nonrelativistic, its position at the time t is $R_h \simeq v_h t/(1+z) = v_h \tilde{t}$, where z is the redshift of the source.[6] Plugging the last expression in Equation (5), we obtain the position of the jet head at the end of the jet lifetime $\tilde{t}_j$,

$$R_h \simeq \left[\frac{\tilde{t}_j^2 \tilde{L}_j^{\rm iso}}{(4\Gamma_h + 3)\pi c \rho_{\rm env,0} R_{\rm env}^2}\right]^{1/2}. \tag{6}$$

[5] We rely on three different reference frames throughout this paper: the CO frame, the observer frame, and the jet comoving frame. In order to distinguish among them, each quantity in each of these frames is denoted as $\tilde{X}$, X, X', respectively.

[6] In the literature, a geometrical correction factor of 2 is often considered in the relations between the radius of the head and the time; see, e.g., He et al. (2018); nevertheless, this does not affect our findings.

If $R_h < R_{\rm ext}$, the jet is choked inside the stellar envelope.

The jet consists of several shells moving with different velocities. This implies that internal shocks (IS; Table 1) may take place in the jet at $R_{\rm IS} \lesssim R_h$, when a fast shell catches up and merges with a slow shell. If $\Gamma_{\rm r} \simeq (\Gamma_{\rm fast}/\Gamma_{\rm merg} + \Gamma_{\rm merg}/\Gamma_{\rm fast})/2$ is the relative Lorentz factor between the fast (moving with $\Gamma_{\rm fast}$) and the merged shell (moving with $\Gamma_{\rm merg}$) in the jet, efficient particle acceleration at the internal shock takes place only if (Murase & Ioka 2013)

$$n_p' \sigma_T R_{\rm IS}/\Gamma \lesssim \min[\Gamma_{\rm r}^2, 0.1 C^{-1}\Gamma_{\rm r}^3], \tag{7}$$

where $C = 1 + 2\ln\Gamma_{\rm r}^2$ is a constant taking into account the pair production, and $n_p' \simeq n_j'$ is the proton density of the unshocked jet material. If Equation (7) is not satisfied, the internal shock is radiative and the particle acceleration is not efficient (Murase & Ioka 2013). We assume that the internal shocks approach the jet head, i.e., $R_{\rm IS} \simeq R_h$ (He et al. 2018).

2.1.1. Photon Energy Distribution

Electrons can be accelerated at the reverse shock between the shocked and the unshocked jet plasma. Then, they heat up and rapidly thermalize due to the high Thomson optical depth of the jet head

$$\tau_{T,h} = n_{e,\rm sh,\,j}\sigma_T \frac{R_h}{\Gamma_h} \gg 1, \tag{8}$$

where $n_{e,\rm sh,\,j} = (4\Gamma_h + 3)n_j'$ is the electron number density of the shocked jet plasma. Therefore, the electrons in the jet head lose all their energy ($\epsilon_e^{\rm RS} e_{{\rm sh},j}$) through thermal radiation, with $e_{{\rm sh},j}$ defined as in Equation (4) and $\epsilon_e^{\rm RS}$ being the fraction of the energy density that goes into the electrons accelerated at the reverse shock. The temperature of the emitted thermal radiation, in the jet head comoving frame, is (Razzaque et al. 2005; Tamborra & Ando 2016)

$$k_B T_h \simeq \left(\frac{30\hbar^3 c^2 \epsilon_e^{\rm RS}\tilde{L}_j^{\rm iso}}{4\pi^4 R_h^2}\right)^{1/4}, \tag{9}$$

with k_B being the Boltzmann constant. Thus, the head appears as a blackbody emitting at temperature $k_B T_{\rm IS}' = \Gamma_{\rm rel} k_B T_h$ in the comoving frame of the unshocked jet. The density of thermal photons in the jet head is

$$n_{\gamma,h} = \frac{19\pi}{(hc)^3}(k_B T_h)^3. \tag{10}$$

As the internal shock approaches the head of the jet, a fraction $f_{\rm esc} = 1/\tau_{T,h}$ of thermal photons escapes in the internal shock (Murase & Ioka 2013), where their number density is boosted by $\Gamma_{\rm rel}$:

$$n_{\gamma,\rm IS}' \simeq \Gamma_{\rm rel} f_{\rm esc}\, n_{\gamma,h}. \tag{11}$$

The resulting energy distribution of thermal photons in the unshocked jet comoving frame is as follows [in units of $\rm GeV^{-1}\,cm^{-3}$]:

$$n_\gamma'(E_\gamma') = \frac{{\rm d}^2 N_\gamma}{{\rm d}E_\gamma' {\rm d}V'} = A_{\gamma,j}' \frac{E_\gamma'^{-2}}{e^{E_\gamma'/(k_B T_{\rm IS}')} - 1}, \tag{12}$$

where $A_{\gamma,j}' = n_{\gamma,\rm IS}'\left[\int_0^\infty dE_\gamma' n_\gamma'(E_\gamma')\right]^{-1}$.

Table 1
Benchmark Input Parameters Characteristic of AT2018cow and CSS161010 Adopted in This Work

Parameter	Symbol	AT2018cow	CSS161010	References
Luminosity distance	d_L	60 Mpc	150 Mpc	[1, 2]
decl.	δ	22°	−8°	[2, 3]
	Choked Jet			
Opening angle	θ_j	0.2	0.2	[4, 5, 6]
Isotropic energy	$\tilde{E}_j^{\rm iso}$ (erg)	10^{50}–10^{52}	10^{50}–10^{52}	[2, 7, 8]
Jet lifetime	$\tilde{t}_j$ (s)	10–10^6	10–10^6	[9, 17]
Lorentz factor	Γ	10–100	10–100	[10, 11, 12]
Dissipation efficiency (IS)	$\epsilon_{\rm d}$	0.2	0.2	[13, 14]
Accelerated proton energy fraction (IS)	$\epsilon_{\rm p}$	0.1	0.1	[15]
Magnetic energy density fraction (IS)	$\epsilon_{\rm B}$	0.1	0.1	[15]
Accelerated electron energy fraction (RS)	$\epsilon_e^{\rm RS}$	0.1	0.1	[16]
	CSM Interaction, Cocoon Model			
Fast outflow velocity	$v_{\rm f}$	$0.2c$	$0.55c$	[2, 6, 7, 18]
Ejecta energy	$\tilde{E}_{\rm ej}$ (erg)	4×10^{48}–10^{51}	6×10^{49}–10^{51}	[2, 7, 18]
Mass-loss rate	$\dot{M}$ ($M_\odot$ yr^{-1})	10^{-4}–10^{-3}	10^{-4}–10^{-3}	[2, 7, 18]
Ejecta mass	$M_{\rm ej}(M_\odot)$	1×10^{-4}–3×10^{-2}	2.2×10^{-4}–4×10^{-3}	[2, 7, 18]
Wind velocity	v_w (km s^{-1})	1000	1000	[2, 7, 18]
CSM radius	$R_{\rm CSM}$ (cm)	1.7×10^{16}	3×10^{17}	[2, 18]
Accelerated proton energy fraction	ϵ_p	0.1	0.1	[19]
Magnetic energy density fraction	ϵ_B	0.01	0.01	[2, 6, 7, 18]
	CSM Interaction, Merger Model			
Fast outflow velocity	$v_{\rm f}$	$0.2c$	0.55 c	[2, 6, 7, 18]
Ejecta energy	$\tilde{E}_{\rm ej}$ (erg)	4×10^{48}–10^{51}	6×10^{49}–10^{51}	[2, 7, 20]
Mass-loss rate	$\dot{M}$ ($M_\odot$ yr^{-1})	7×10^{-6}–7×10^{-5}	7×10^{-6}–7×10^{-5}	[2, 7, 20]
Ejecta mass	$M_{\rm ej}(M_\odot)$	10^{-4}–3×10^{-2}	2.2×10^{-4}–4×10^{-3}	[2, 7, 20]
Wind velocity	v_w (km s^{-1})	10	10	[20]
CSM radius	$R_{\rm CSM}$ (cm)	3×10^{16}	3×10^{16}	[20]
Accelerated proton energy fraction	ϵ_p	0.1	0.1	[19]
Magnetic energy density fraction	ϵ_B	0.01	0.01	[2, 6, 7, 18]

Note. Some parameters are inferred from observations, while others denote typical values derived on theoretical grounds or by combining observations and theoretical arguments. The following references are quoted in the table: [1] Prentice et al. (2018), [2] Coppejans et al. (2020), [3] Perley et al. (2019), [4] Granot (2007), [5] Kumar & Zhang (2014), [6] A. J. & Chandra (2021), [7] Margutti et al. (2019), [8] Gottlieb et al. (2022b), [9] Ostriker & Gunn (1969), [10] Mizuta & Ioka (2013), [11] Meszaros & Waxman (2001), [12] Tan et al. (2001), [13] Kobayashi et al. (1997), [14] Guetta et al. (2001), [15] Sironi & Spitkovsky (2011), [16] He et al. (2018), [17] Kippenhahn et al. (1990), [18] Ho et al. (2019), [19] Caprioli & Spitkovsky (2014), [20] Metzger (2022).

2.1.2. Proton Energy Distribution

Protons are accelerated to a power-law distribution at the internal shock, even though the mechanism responsible for particle acceleration is still under debate (e.g., Sironi et al. 2013; Guo et al. 2014; Nalewajko et al. 2015; Petropoulou & Sironi 2018; Kilian et al. 2020). The injected proton distribution in the jet comoving frame is [in units of GeV^{-1} cm^{-3}]

$$n'_p(E'_p) \equiv \frac{{\rm d}^2 N'_{\rm p}}{{\rm d}E'_{\rm p}{\rm d}V'} = A'_p E_p^{'-k_p} \times \exp\left[-\left(\frac{E'_p}{E'_{p,\rm max}}\right)^{\alpha_p}\right]\Theta(E'_p - E'_{p,\rm min}), \quad (13)$$

where k_p is the proton spectral index, $\alpha_p = 1$ simulates an exponential cutoff (Malkov & Drury 2001), and Θ is the Heaviside function. The value of k_p is highly uncertain: it is estimated to be $k_p \simeq 2$ from the nonrelativistic shock diffusive acceleration theory (Matthews et al. 2020), while it is expected to be $k_p \simeq 2.2$ from Monte Carlo simulations of ultra-relativistic shocks (Sironi et al. 2013). In this work, we assume $k_p \simeq 2$.

The normalization constant is $A'_p = \epsilon_p \epsilon_{\rm d} e'_j \left[\int_{E'_{p,\rm min}}^{E'_{p,\rm max}} dE'_p E'_p n'_p(E'_p)\right]^{-1}$, where $\epsilon_{\rm d}$ is the fraction of the comoving internal energy density of the jet $e'_j = \tilde{L}_j^{\rm iso} / (4\pi R_{\rm IS}^2 c \Gamma^2)$, which is dissipated at the internal shock, while ϵ_p is the fraction of this energy that goes in accelerated protons. We rely on a one-zone model for the emission from internal shocks and omit any radial evolution of the properties of the colliding shells. Hence, we assume that the dissipation efficiency $\epsilon_{\rm d}$ is constant (e.g., Guetta et al. 2001; Pitik et al. 2021). Note, however, that $\epsilon_{\rm d}$ depends on the details of the collision, i.e., the relative Lorentz factor between the colliding shells and their mass (see, e.g., Daigne & Mochkovitch 1998; Kobayashi et al. 1997).

The minimum energy of accelerated protons is $E'_{p,\rm min} = m_p c^2$, while $E'_{p,\rm max}$ is the maximum energy up to which protons can be accelerated at the internal shock. The latter is fixed by the condition that the proton acceleration timescale $t'^{-1}_{p,\rm acc}$ is smaller than the total cooling timescale $t'^{-1}_{p,\rm cool}$. For details on the cooling timescales of protons, see Appendix.

At the internal shock, the fraction ϵ_B of the dissipated jet internal energy is given to the magnetic field: $B' = \sqrt{8\pi\epsilon_B\epsilon_{\rm d}e'_j}$.

2.2. Interaction with the Circumstellar Medium

While the presence of a choked jet is uncertain because of the lack of electromagnetic evidence (Bietenholz et al. 2020), the existence of fast ejecta launched by the central engine and moving with $v_{\rm f}\gtrsim 0.1c$ is supported by observations in the radio band.[7] The origin of the ejecta is still unclear and under debate. In the following, we discuss several viable mechanisms for the production of a fast outflow expanding outwards in the CSM.

1. In the cocoon model presented in Gottlieb et al. (2022b; see left panels of Figure 1), as the jet propagates in the stellar envelope (Section 2.1), a double-layered structure, the cocoon, forms around the jet; see, e.g., Bromberg et al. (2011). The cocoon breaks out from the star and expands in the surrounding CSM (Gottlieb et al. 2022a). The interaction between the CSM and the cocoon is responsible for the observed radio signal. It is expected that the cocoon's ejecta are stratified in velocity, and the fastest component propagates with $v_{\rm f}\gtrsim 0.1c$. Since we assume that the jet is choked in the extended stellar envelope and far from the stellar core, the fast component of the cocoon does not have any relativistic component moving with Lorentz factor $\Gamma_{\rm f}\sim 3$ (Gottlieb et al. 2022a). In addition to the fast ejecta, the outflow contains a slow component moving with $v_{\rm s}\lesssim 0.01c$. This component might be the slow part of the SN ejecta accompanying the jet launching. Note that there might be a faster component of the SN ejecta, but the radio signal is probably dominated by the cocoon emission (Gottlieb et al. 2022b).
2. The merger model proposed in Metzger (2022; see right panels of Figure 1) invokes a Wolf–Rayet–black hole merger following a failed common envelope phase. This leads to a highly asymmetric CSM: a very dense region extends up to $R\simeq 10^{14}$ cm around the equator, and a less dense component extends up to $R\simeq 10^{16}$ cm in the polar direction. The asymmetric CSM is clearly required by electromagnetic observations of AT2018cow (Margutti et al. 2019) and the energetics of the fastest ejecta of CSS161010 (Coppejans et al. 2020). An accretion disk forms as a result of the merger; slow ejecta in the equatorial direction move with $v_{\rm s}\simeq 0.01c$, and the fast component in the polar plane has $v_{\rm f}\simeq 0.1c$.

Two other models have been proposed in the literature with features similar to the ones of the scenarios described above for what concerns the neutrino production. Lyutikov (2022) suggests that LFBOTs arise from the accretion induced collapse of a binary–double white dwarf merger. In this case, neutrinos may be produced at the highly magnetized and highly relativistic wind termination shock, responsible for the observed radio emission. In this scenario, we expect a neutrino signal similar to the one of the cocoon model (from CSM interaction only), because of the similarity with the model parameters considered in Lyutikov (2022). Soker (2022) invokes a common envelope phase between a red supergiant and a CO. This mechanism shares common features with the one proposed in Gottlieb et al. (2022b). Nevertheless, while the former predicts baryon-loaded jets, the latter invokes relativistic jets. The neutrino production from the jet model proposed in Soker (2022) may mimic the results obtained in Grichener & Soker (2021). Moreover, as for the scenario of Metzger (2022), a common envelope phase, during which an asymmetric CSM forms, is proposed. The parameters obtained in the common envelope jet SN impostor scenario are similar to the cocoon model as for the total energy and mass of the ejecta, as well as for the CSM properties. Results similar to the ones of the cocoon model should hold for the common envelope jet SN impostor scenario, when taking into account CSM interaction. Hence, in the following, we focus on the cocoon and merger models only.

Independently of its origin, the fast outflow propagates outwards in the surrounding CSM, giving rise to the observed radio spectrum. Observations suggest a certain degree of asymmetry in the LFBOTs outflows (Margutti et al. 2019; Coppejans et al. 2020; Yao et al. 2022). Nevertheless, for the sake of simplicity, we consider a spherically symmetric geometry both for the ejecta and the CSM. We parameterize the CSM with a wind profile

$$n_{p,\rm CSM}(R) = \frac{\dot{M}}{4\pi m_p v_w R^2}, \tag{14}$$

where $\dot{M}$ is the mass-loss rate of the star and v_w is the wind velocity. The CSM extends up to $R_{\rm CSM}$, and its mass is obtained by integrating Equation (14) over the volume of the CSM shell, $\mathrm{d}V_{\rm CSM} = 4\pi R^2\mathrm{d}R$. Note however that radio observations of AT2018cow indicate a steeper density profile for the CSM; see, e.g., A. J. & Chandra (2021). Here, we assume a standard wind profile for a general case.

As the outflow expands in the CSM, forward and reverse shocks form—propagating in the stellar wind and back to the ejecta in mass coordinates, respectively. Both the forward and reverse shocks contribute to neutrino production. On the basis of similarities with the SN scenario, the forward shock is expected to be the main dissipation site of the kinetic energy of the outflow (e.g., Ellison et al. 2007; Patnaude & Fesen 2009; Schure et al. 2010; Suzuki et al. 2020; Slane et al. 2014; Sato et al. 2018); hence, we focus on the forward shock only, which moves with speed $v_{\rm sh}\simeq v_{\rm f}$.

If the outflow expands in a dense CSM with optical depth $\tau_{\rm CSM}$, the forward shock is radiation mediated as long as $\tau_{\rm CSM}\gg 1$ and the particle acceleration is not efficient (Levinson & Bromberg 2008; Katz et al. 2011; Murase et al. 2011). Radiation escapes at the breakout radius $R_{\rm bo}$, when the optical depth drops below $v_{\rm sh}/c$. The breakout radius is obtained by solving the following equation:

$$\tau_{\rm CSM} = \int_{R_{\rm bo}}^{R_{\rm CSM}} dr\ \sigma_T n_{p,\rm CSM}(R) = \frac{c}{v_{sh}}. \tag{15}$$

Existing data suggest that the LFBOT ejecta were possibly slowly decelerating during the time of observations (e.g., Coppejans et al. 2020). Nevertheless, this behavior is not well probed, and the treatment of the deceleration of a mildly relativistic blastwave is not straightforward (Coughlin 2019). Hereafter, we assume that the shock freely moves with constant

[7] It is worth noticing that the speed for the ejecta is very similar to the one of core-collapse SNe. Nevertheless, LFBOTs have been observed with fast ejecta speeds up to $v_{\rm f}\simeq 0.6c$; see, e.g., Coppejans et al. (2020). This feature makes these transients different from core-collapse SNe.

speed $v_{\rm sh}$ up to the deceleration radius

$$R_{\rm dec} = R_{\rm bo} + \frac{M_{\rm ej}}{4\pi m_p n_{p,\rm bo} R_{\rm bo}^2}, \quad (16)$$

where $M_{\rm ej}$ is the mass of the ejecta, and $n_{p,\rm bo} = n_{p,\rm CSM}(R_{\rm bo})$. At this radius, the ejecta have swept up a mass comparable to $M_{\rm ej}$ from the CSM.

2.2.1. Proton Energy Distribution

Diffusive shock acceleration of the CSM protons occurs at $R \gtrsim R_{\rm bo}$, and the accelerated protons are assumed to have a power-law energy distribution. For a wind-like CSM, the proton distribution reads [in units of $\rm GeV^{-1}\ cm^{-3}$]

$$\tilde{n}_p(\tilde{E}_p) \equiv \frac{{\rm d}^2\tilde{N}_p}{{\rm d}\tilde{E}_p {\rm d}\tilde{V}} = \tilde{A}_p \tilde{E}_p^{-k_p} \Theta(\tilde{E}_p - \tilde{E}_{p,\rm min})\Theta(\tilde{E}_{p,\rm max} - \tilde{E}_{\rm p}); \quad (17)$$

as for the choked jet scenario, we fix the proton spectral index $k_p = 2$. Moreover, the minimum energy of protons is $\tilde{E}_{p,\rm min} = m_p c^2$, since these shocks are not relativistic. The maximum energy of the shock-accelerated protons is fixed by the condition that the acceleration timescale is shorter than the total cooling timescale, i.e., $\tilde{t}_{\rm acc}^{-1} \geqslant \tilde{t}_{\rm cool}^{-1}$ (see Appendix). Note that for CSM interaction there is no difference between the comoving frame of the shock and the CO frame, since the involved speeds are subrelativistic. Hence, the primed quantities are equivalent to the twiddled ones.

$\tilde{A}_p = 9\epsilon_p n_{p,\rm CSM}(R) m_p c^2 / [8 \ln(\tilde{E}_{p,\rm max}/\tilde{E}_{p,\rm min})](v_{\rm sh}/c)^2$ is the normalization constant. Here, ϵ_p is the fraction of the post-shock internal energy, $\tilde{e}_{\rm th} = 9 m_p c^2 (v_{\rm sh}/c)^2 n_{p,\rm CSM}(R)/8$, that goes in accelerated protons. The fraction ϵ_B of $\tilde{e}_{\rm th}$ is instead stored in the magnetic field generated at the forward shock: $\tilde{B} = \sqrt{9\pi\epsilon_B m_p c^2 (v_{\rm sh}/c)^2 n_{p,\rm CSM}(R)}$. We stress that the quantities introduced so far for CSM interaction evolve with the radius of the expanding outflow, and hence with time.

Electrons are expected to be accelerated together with protons at the forward shock and produce the synchrotron self-absorption spectrum observed in the radio band. The electron population responsible for the radio emission is still under debate (Ho et al. 2021; Margalit & Quataert 2021). Nevertheless, we verified that $p\gamma$ interactions are negligible for a wide range of parameters, consistently with the results reported in Murase et al. (2011); Fang et al. (2020). Hence, we do not introduce any photon distribution and neglect the neutrino production through $p\gamma$ interactions in the context of CSM–ejecta interaction (see Section 4).

3. Benchmark Luminous Fast Blue Optical Transients: AT2018cow and CSS161010

In this section, we provide an overview on the parameters characteristic of AT2018cow and CSS161010. We select these two transients as representative of the detected LFBOTs for two reasons. First, they are the closest ones ($d_L \simeq 60$ Mpc for AT2018cow and $d_L \simeq 150$ Mpc for CSS161010; d_L is the luminosity distance, defined as in Section 4.3); second, while these two LFBOTs share similar CSM densities, an extension of the CSM, ejecta mass, and kinetic energy as the population of LFBOTs, their fastest ejecta span the entire range of values inferred. AT2018cow showed $v_{\rm f} \simeq 0.1$–$0.2c$ (Margutti et al. 2019; Ho et al. 2019; A. J. & Chandra 2021), while CSS161010 is the fastest LFBOT observed to date with $v_{\rm f} \simeq 0.55c$ (Coppejans et al. 2020). We fix the speed of the fastest component of the outflow as measured from observations. The other characteristic parameters are still uncertain; hence we vary them within an uncertainty range. The parameters adopted for the choked jet (opening angle θ_j, Lorentz factor Γ, and lifetime $\tilde{t}_j$) are fixed on the basis of theoretical arguments as justified below. The typical parameters adopted for the choked jet and for CSM interaction are summarized in Table 1.

As for the cocoon model harboring a choked jet, $\tilde{E}_j = \tilde{L}_j \tilde{t}_j$ corresponds to the physical energy injected by the central engine into the jet, whose opening angle is assumed to be $\theta_j = 0.2$ rad (e.g., Granot 2007; Kumar & Zhang 2014). Since the jet is choked, all of its energy is transferred to the cocoon, i.e., the cocoon breaks out with energy $\tilde{E}_{\rm ej} \simeq \tilde{E}_j$; note that, in principle, we should consider that a fraction of the jet energy is dissipated at the internal shocks; nevertheless this fraction is small enough to be negligible [$\sim$10%; Kobayashi et al. 1997]. The kinetic energy $\tilde{E}_k$ of the ejecta interacting with the CSM has been estimated from the radio data, and it represents a lower limit on the total energy of the outflow, $\tilde{E}_{\rm ej}$ (see "CSM Interaction, Cocoon Model" in Table 1). The upper limit on the total energy of the outflow is not directly inferred from observations, but estimations of its range of variability have been attempted. Thus, we vary the energy injected in the jet in the interval spanned by the lower and upper limits of the outflow energy, obtained by combining observations and theoretical assumptions (see "Choked Jet" in Table 1 and references therein). As mentioned in Section 2.1, the dynamics of the jet are conveniently described by the isotropic equivalent quantities; we refer to the isotropic equivalent energy of the jet: $\tilde{E}_j^{\rm iso} = \tilde{E}_j / (\theta_j^2/4)$.

The Lorentz factor of the jet is not measured. Hence, we rely on two extreme cases: $\Gamma = 10$ and 100. This choice is due to the fact that numerical simulations and semianalytical models suggest that the jet propagates in the stellar core with $\Gamma \simeq 1$–10 (Mizuta & Ioka 2013; Harrison et al. 2018). Nevertheless, when the jet pierces the stellar core at $R_\star \simeq 10^{11}$ cm and enters the extended envelope, it may be accelerated up to $\Gamma \lesssim 100$ because of the sudden drop in density (Meszaros & Rees 2001; Tan et al. 2001).

The jet lifetime is linked to the CO physics. The CO harboring relativistic jets can be either a black hole (Gottlieb et al. 2022a; Quataert et al. 2019) or a millisecond magnetar (Metzger et al. 2011). If we assume that the central engine of LFBOTs is a magnetar with initial spin period $_{Pi}$, magnetic field B_m, and mass $M_m = 1.4 M_\odot$, then the upper limit on the jet lifetime is set by the spin-down period (Ostriker & Gunn 1969):

$$\tilde{t}_{\rm sd} = 2.0 \times 10^5\ {\rm s} \left(\frac{P_i}{10^{-3}\ {\rm s}}\right)^2 \left(\frac{B_m}{10^{14}\ {\rm G}}\right)^2. \quad (18)$$

Following Fang et al. (2019), for $P_i = 10$ ms and $B_m = 10^{15}$ G, we obtain $\tilde{t}_j \lesssim \tilde{t}_{\rm sd} = 2 \times 10^5$ s. If the CO is a black hole, the upper limit on the jet lifetime is set by the freefall time of the stellar material (Kippenhahn et al. 1990):

$$\tilde{t}_{\rm ff} \simeq 1.7 \times 10^7\ {\rm s} \left(\frac{R_{\rm BH}}{10^{13.5}\ {\rm cm}}\right)^{3/2} \left(\frac{M_{\rm BH}}{M_\odot}\right)^{-1/2}, \quad (19)$$

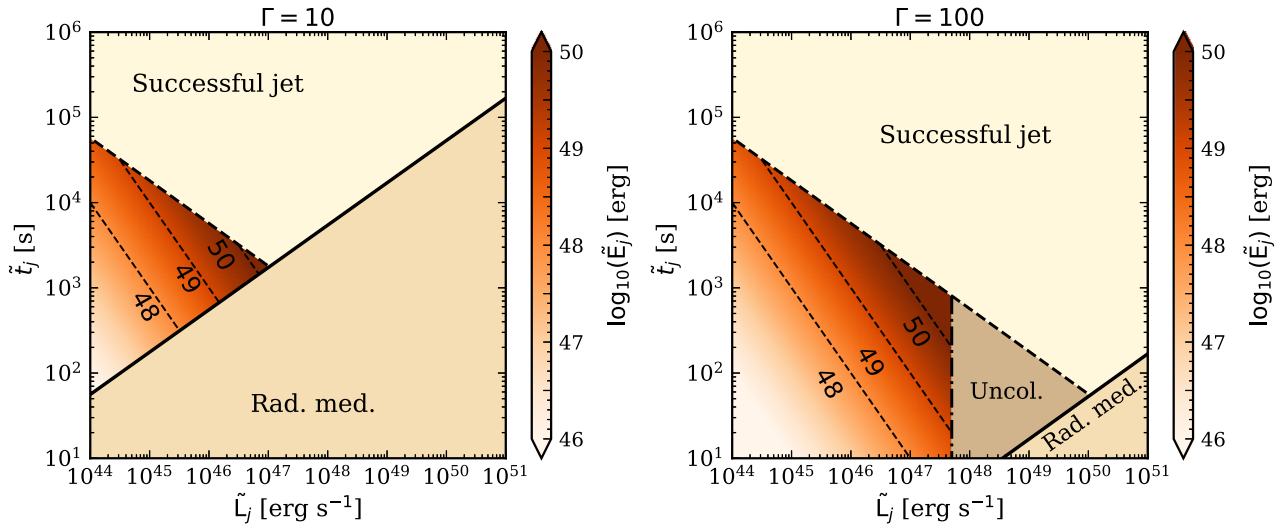

Figure 2. Contour plot of the energy injected in the jet by the central engine ($\tilde{E}_j = \tilde{L}_j \tilde{t}_j$) in the plane spanned by $\tilde{L}_j$ and $\tilde{t}_j$ for $\Gamma = 10$ (left panel) and $\Gamma = 100$ (right panel). The light-yellow region is excluded since it would give rise to a successful jet. The light-brown region in the right lower corner is excluded because the jet would be radiation mediated ("Rad. med."; see, Equation (7)). For $\Gamma = 100$, we exclude an additional region corresponding to an uncollimated jet ("Uncol"; brown region in the right panel). In the allowed region of the parameter space, the black-dashed lines are meant to guide the eye and correspond to $\tilde{E}_j = 10^{48}$, 10^{49}, 10^{50} erg.

where $M_{\rm BH}$ is the black hole mass, and $R_{\rm BH}$ is the distance from it. Since the nature of the CO powering LFBOTs as well as the presence of a jetted outflow is uncertain, we vary the jet lifetime in $\tilde{t}_j \in [10,\ 10^6]$ s. Note, however, that a short lifetime ($\tilde{t}_j < 10^3$ s) may require an amount of energy released by the CO larger than the sum of the observed radiated energy and the kinetic energy of the ejecta. This consideration arises when extrapolating the X-ray lightcurve—likely associated with the CO powering LFBOTs (e.g., Margutti et al. 2019; Coppejans et al. 2020)—back to early times ($\tilde{t} \sim \tilde{t}_j$). Nevertheless, there is no robust signature that allows us to confidently exclude shorter CO lifetimes. Hence, we choose to span a wide range for $\tilde{t}_j$. Finally, the microphysical parameters ϵ_B, ϵ_p, and $\epsilon_e^{\rm RS}$ are fixed to typical values of choked jets; see "Choked Jet" in Table 1 and references therein.

Note that the same energy $\tilde{E}_j$ can be injected from the CO for different ($\tilde{L}_j$, $\tilde{t}_j$) pairs. Since our main goal is to explore viable mechanisms for neutrino production in LFBOTs, not all ($\tilde{L}_j$, $\tilde{t}_j$) pairs are allowed, as shown in Figure 2. In fact, the ($\tilde{L}_j$, $\tilde{t}_j$) pairs that do not satisfy, simultaneously, the choked jet condition ($R_h < R_{\rm ext}$, with R_h given by Equation (6)) and the acceleration constraint in Equation (7) are excluded. Examples of the allowed ($\tilde{L}_j$, $\tilde{t}_j$) pairs are shown in Figure 2 for $\Gamma = 10$ and 100. We also exclude the ($\tilde{L}_j$, $\tilde{t}_j$) pairs leading to an uncollimated jet in the extended envelope for the fixed θ_j, as suggested by numerical simulations and implied by observations (Gottlieb et al. 2022b); see Bromberg et al. (2011); Xiao & Dai (2014) for details.[8] Uncollimated outflows are ruled out by energetic considerations, since they would require a total energy of the ejecta, $\tilde{E}_{\rm ej} \simeq 10^{53}$ erg, much larger than the one estimated for LFBOTs, i.e., $\tilde{E}_{\rm ej} \simeq 10^{50}$–$10^{51}$ erg (Coppejans et al. 2020; Ho et al. 2020, 2019). In Figure 2, we consider isocontours of the isotropic energy $\tilde{E}_j$ in the ($\tilde{L}_j$, $\tilde{t}_j$) parameter space . Note that, for $\Gamma = 10$, the region excluded from the collimation argument overlaps with the area already excluded; therefore, we do not show it explicitly.

Concerning CSM interaction occurring in the cocoon model, if $v_{\rm f}$ is the speed of the fastest component of the cocoon responsible for the observed radio emission and $E_k = \tilde{E}_k/(1+z)$ is its kinetic energy, its mass $M_{\rm ej}$ can be obtained through the following relation

$$v_{\rm ej} = \sqrt{\frac{2E_k}{M_{\rm ej}}}. \tag{20}$$

We then vary $M_{\rm ej}$ in the range corresponding to the upper and lower limits on the kinetic energy of the outflow. The former is obtained by assuming that all the energy of the ejecta is converted into kinetic energy, i.e., $\tilde{E}_k = \tilde{E}_{\rm ej}$; the latter is constrained from observations. The range of variability of $M_{\rm ej}$ is shown in Table 1 for AT2018cow and CSS161010 (see under "CSM Interaction, Cocoon Model"). The mass-loss rate $\dot{M}$ spans the range hinted from radio data, while the CSM radius is fixed from the latest radio observations; see "CSM interaction, Cocoon Model" in Table 1 and references therein.

For the merger model, we fix the upper limit on the total energy of the ejecta at the theoretical value estimated by Metzger (2022). We instead vary the mass of the fast ejecta by using Equation (20), following the argument reported above concerning the upper and lower limits on the kinetic energy. Finally, the mass-loss rate spans a range obtained from theoretical predictions of the model, while the extension of the CSM is fixed from theoretical estimations (Metzger 2022). All the aforementioned parameters and their variability ranges are listed in the section "CSM Interaction, Merger Model" of Table 1.

[8] We assume a density profile of the stellar core $\rho_{\rm star}(R) = M_\star/(4\pi R_\star)R^{-2}$, valid up to the He envelope; this profile follows Matzner & McKee (1999); Xiao & Dai (2014) for progenitors harboring choked jets. For the mass of the stellar core and its radius we use $M_\star = 4M_\odot$ and $R_\star = 6 \times 10^{11}$ cm, respectively, inspired by Gottlieb et al. (2022b) that reproduces the lightcurve of AT2018cow.

4. Neutrino Production

In this section, we summarize the viable mechanisms for neutrino production in LFBOTs. In particular, we discuss the interactions between the shock-accelerated protons and target photons at the internal shocks ($p\gamma$ interactions) in the choked jet and interactions between the shock-accelerated protons and a steady target of protons (pp interactions), taking place when the outflow expands in the CSM. In both cases, we present the procedure adopted to compute the high-energy neutrino flux at Earth.

4.1. Neutrino Production via Proton–Photon Interactions

Protons accelerated at the internal shocks interact with the thermal photons escaping from the jet head and going back to the unshocked jet. Efficient $p\gamma$ interactions take place at the internal shock, mainly through the Δ^+ channel

$$p + \gamma \longrightarrow \Delta^+ \longrightarrow \begin{cases} n + \pi^+ & 1/3 \text{ of all cases} \\ p + \pi^0 & 2/3 \text{ of all cases,} \end{cases} \tag{21}$$

while we can safely neglect pp interactions at the internal shocks, since they are subleading (see Appendix). The reaction channel in Equation (21) is followed by the decay of neutral pions into photons: $\pi^0 \longrightarrow 2\gamma$. At the same time, neutrinos can be copiously produced in the decay chain $\pi^+ \longrightarrow \mu^+ + \nu_\mu$, followed by the muon decay $\mu^+ \longrightarrow \bar{\nu}_\mu + \nu_e + e^+$.

We rely on the photohadronic model presented in Hummer et al. (2010). Hence, given the injected energy distribution of protons $[n'_p(E'_p)]$ and the distribution of target photons $[n'_\gamma(E'_\gamma)]$, the rate of production of secondary particles l (with $l = \pi^\pm, \pi^0, K^+$) in the comoving frame of the unshocked jet is given by the following [in units of $\mathrm{GeV}^{-1}\,\mathrm{cm}^{-3}\,\mathrm{s}^{-1}$]:

$$Q'_l(E'_l) = c \int_{E'_l}^{\infty} \frac{dE'_p}{E'_p} n'(E'_p) \int_{E_{\rm th}/2\gamma'_p}^{\infty} dE'_\gamma n'_\gamma(E'_\gamma) R(x, y), \tag{22}$$

where $x = E'_l/E'_p$ is the fraction of proton energy that is given to secondary particles, $y = \gamma'_p E'_l$, and $R(x, y)$ is the response function, which contains the physics of the interaction. The initial distributions of protons and photons are given by Equations (13) and (12), respectively.

Before decaying, each charged meson l undergoes energy losses, parameterized through the cooling time $t'^{-1}_{l,\rm cool}$; see Appendix. Therefore, the spectrum at the decay is

$$Q'^{\rm dec}_l(E'_l) = Q'_l(E'_l)\left[1 - \exp\left(-\frac{t'_{l,\rm cool} m_l}{E'_l \tau'_l}\right)\right], \tag{23}$$

where τ'_l is the lifetime of the meson l. The comoving neutrino spectrum from the decayed mesons is as follows [in units of $\mathrm{GeV}^{-1}\,\mathrm{cm}^{-3}\,\mathrm{s}^{-1}$]:

$$Q'_{\nu_\alpha}(E'_\nu) = \int_{E'_\nu}^{\infty} \frac{dE'_l}{E'_l} Q'^{\rm dec}_l(E'_l) F_{l\to\nu_\alpha}\left(\frac{E'_\nu}{E'_l}\right), \tag{24}$$

where $\alpha = e, \mu$ is the neutrino flavor at production, and $F_{l\to\nu_\alpha}$ is provided in Lipari et al. (2007). We use $\nu_\alpha \equiv \nu_\alpha + \bar{\nu}_\alpha$, i.e., we do not distinguish between neutrinos and antineutrinos.

Magnetic fields in the internal shock are not large enough to efficiently cool kaons, which have a larger mass and a shorter lifetime compared to pions and muons. Therefore, they suffer less energy losses and do not contribute significantly to the neutrino spectrum, even though they may become important at high energies (He et al. 2012; Asano & Nagataki 2006; Petropoulou et al. 2014; Tamborra & Ando 2015).

4.2. Neutrino Production via Proton–Proton Interactions

Similar to SNe, the stellar outflows interacting with dense CSM can be neutrino factories (Murase et al. 2011; Pitik et al. 2022; Petropoulou et al. 2017, 2016; Katz et al. 2011; Murase et al. 2014; Cardillo et al. 2015; Zirakashvili & Ptuskin 2016; Murase et al. 2020; Sarmah et al. 2022), when the protons accelerated at the forward shock between the ejecta and the CSM interact with the steady target of protons of the CSM.

Given the population of injected shock-accelerated protons in Equation (17), the proton distribution evolves as follows (Sturner et al. 1997; Finke & Dermer 2012; Petropoulou et al. 2016):

$$\frac{\partial \tilde{N}_{\rm p}(\tilde{\gamma}_{\rm p}, R)}{\partial R} - \frac{\partial}{\partial \tilde{\gamma}_{\rm p}}\left[\frac{\tilde{\gamma}_{\rm p}}{R}\tilde{N}_{\rm p}(\tilde{\gamma}_{\rm p}, R)\right] + \frac{\tilde{N}_{\rm p}(\tilde{\gamma}_{\rm p}, R)}{v_{\rm sh}\tilde{t}_{pp}(R)} = \tilde{Q}(\tilde{\gamma}_p), \tag{25}$$

where $\tilde{N}_{\rm p}(\tilde{\gamma}_{\rm p}, R)$ is the total number of protons with Lorentz factor between $\tilde{\gamma}_p$ and $\tilde{\gamma}_p + d\tilde{\gamma}_p$ contained in the shell of shocked material at radius R, and $\tilde{Q}(\tilde{E}_p) = \pi R_{\rm bo}^2 \tilde{n}(\tilde{E}_p/m_p c^2, R = R_{\rm bo})/(m_p c^2)$ is the proton injection rate at the breakout radius [in units of per centimeter]. The second term on the left-hand side of Equation (25) parameterizes the adiabatic losses due to the expansion of the shocked shell, while the third term corresponds to pp collisions, treated as an escape term (Sturner et al. 1997).

The neutrino production rates for neutrinos of flavor α, Q_{ν_α}, are given by the following (in units of $\mathrm{GeV}^{-1}\,\mathrm{cm}^{-1}$; Kelner et al. 2006):

$$\tilde{Q}_{\nu_\alpha}(\tilde{E}_\nu, R) = \frac{4 n_{p,\rm CSM}(R) m_p c^3}{v_{\rm sh}} \int_0^1 dx \frac{\sigma_{pp}(\tilde{E}_\nu/x)}{x} \times \tilde{N}_{\rm p}\left(\frac{\tilde{E}_\nu}{x m_{\rm p} c^2}, R\right) F_{\nu_\alpha}(\tilde{E}_\nu, x), \tag{26}$$

where $x = \tilde{E}_\nu/\tilde{E}_{\rm p}$, and the function F_{ν_α} is provided in Kelner et al. (2006). Note that Equation (26) is only valid for $E_{\rm p} > 0.1$ TeV, which is the energy range we are interested in.

4.3. Neutrino Flux at Earth

On their way to Earth, neutrinos undergo flavor conversion. The observed distribution for the flavor ν_α (with $\alpha = e, \mu, \tau$) is [in $\mathrm{GeV}^{-1}\,\mathrm{cm}^{-2}\,\mathrm{s}^{-1}$]

$$F_{\nu_\alpha}(E_\nu, z) = \mathcal{T}\frac{(1+z)^2}{4\pi d_L^2(z)} \sum_\beta P_{\nu_\beta\to\nu_\alpha}(E_\nu)\, \mathcal{Q}'_{\nu_\beta}(E_\nu \mathcal{L}), \tag{27}$$

with $\mathcal{Q}'_{\nu_\beta}(E_\nu \mathcal{L})$ being the neutrino production rate in the comoving jet ($p\gamma$ interactions) or in the center of the explosion (pp interactions) frame, given by Equations (24) and (26), respectively. The constant $\mathcal{T} = V'_{\rm iso} = 4\pi R'^3_{\rm IS}/(2\Gamma)$ represents the isotropic volume of the interaction region (Baerwald et al. 2012) in the choked jet scenario, while $\mathcal{T} = v_{\rm sh}$ for CSM–ejecta interaction. Note that $\mathcal{T}$ has different dimensions in the choked jet scenario compared to the CSM–ejecta interaction case,

because of the different dimensionality of the corresponding neutrino injection rates; see, Equations (24) and (26). Moreover, the Lorentz conversion factor is $\mathcal{L} = (1+z)/\Gamma$ for the choked jet and $\mathcal{L} = (1+z)$ for CSM interaction. The neutrino oscillation probability $P_{\nu_\beta \to \nu_\alpha} = P_{\bar{\nu}_\beta \to \bar{\nu}_\alpha}$ is given by the following (Anchordoqui et al. 2014; Farzan & Smirnov 2008):

$$P_{\nu_e \to \nu_\mu} = P_{\nu_\mu \to \nu_e} = P_{\nu_e \to \nu_\tau} = \frac{1}{4}\sin^2 2\theta_{12}, \tag{28}$$

$$P_{\nu_\mu \to \nu_\mu} = P_{\nu_\mu \to \nu_\tau} = \frac{1}{8}(4 - \sin^2\theta_{12}), \tag{29}$$

$$P_{\nu_e \to \nu_e} = 1 - \frac{1}{2}\sin^2 2\theta_{12}, \tag{30}$$

with $\theta_{12} \simeq 33^\circ.5$ (Particle Data Group et al. 2020; Esteban et al. 2020). The luminosity distance in a standard flat ΛCDM cosmology is as follows:

$$d_L(z) = (1+z)\frac{c}{H_0}\int_0^z \frac{dz'}{\sqrt{\Omega_\Lambda + \Omega_M(1+z')^3}}, \tag{31}$$

where we use $H_0 = 67.4\ \mathrm{km\,s^{-1}\,Mpc^{-1}}$, $\Omega_M = 0.315$, and $\Omega_\Lambda = 0.685$ (Aghanim et al. 2020; Particle Data Group et al. 2020).

The neutrino fluence at Earth is

$$\Phi_{\nu_\alpha}(E_\nu) = \int_{t_i}^{t_f} dt\ F_{\nu_\alpha}(E_\nu, t), \tag{32}$$

where $F_{\nu_\alpha}(E_\nu, t)$ is given by Equation (27), t_i and t_f are the onset and final times of neutrino production, respectively, measured by an observer at Earth. For the choked jet scenario, the integral in Equation (32) is replaced by the product with the jet lifetime t_j. For CSM interaction, we fix the onset of our calculations $t_i \equiv t_{\rm bo} = (1+z)R_{\rm bo}/v_{\rm sh}$ and follow the neutrino signal up to $t_f \equiv t_{\rm ext} = (1+z)R_{\rm ext}/v_{\rm sh}$, where $R_{\rm ext} = \min[R_{\rm CSM}, R_{\rm dec}]$. In the last expression, $R_{\rm dec}$ is given by Equation (16). This choice is justified because efficient particle acceleration takes place for $R \gtrsim R_{\rm bo}$ only; hence, no neutrinos can be produced before the breakout occurs. Second, for $R \gtrsim R_{\rm ext}$, either the CSM ends and there are no longer target protons for *pp* interactions to occur or the ejecta start to be decelerated and the neutrino signal quickly drops as $\propto v_{\rm sh}^2$ (Petropoulou et al. 2016). Therefore, neutrino production is no longer efficient.

Both the cocoon model and the merger model predict the presence of slow ejecta, with $v_{\rm s} \simeq 0.01c$. Nevertheless, the fast component of the ejecta in the cocoon model sweeps up the CSM around the star; therefore, when the slow component emerges, there are no longer target protons for efficient *pp* interactions to occur (in the assumption of spherical symmetry). As for the merger model, the slow outflow propagates into a highly dense and compact CSM. However, shocks in the equatorial region are radiative, and the neutrinos should be produced with a maximum energy lower than the one of the neutrinos produced in the fast outflow–CSM interaction (see, e.g., Fang et al. 2020). Furthermore, the equatorial CSM has a smaller extension than the polar one, and the corresponding neutrino production would last for a shorter time. As a consequence, we consider the neutrino signal from the fast outflow only.

5. Neutrino Signal from Nearby Sources

In this section, we present our forecasts for the neutrino signal for the the choked and CSM interaction models. We also discuss the number of neutrinos expected at the IceCube Neutrino Observatory as well as the detection perspectives at upcoming neutrino detectors, such as IceCube-Gen2.

5.1. Neutrino Fluence

For the choked jet scenario (see Section 2.1), for the fixed isotropic equivalent energy $\tilde{E}_j^{\rm iso}$, we consider an envelope containing the expected neutrino fluence for the allowed $(\tilde{L}_j, \tilde{t}_j)$ pairs. As for CSM interaction in the cocoon model, we fix $R_{\rm bo} = R_{\rm env} = 3 \times 10^{13}$ cm up to $R_{\rm ext}$. Indeed, in the hypothesis of an extended stellar envelope surrounding the core of the star, the CSM is already optically thin at the edge of the envelope, and radiation can escape as soon as the cocoon breaks out. As already pointed out, in the merger model, the breakout radius is calculated by using Equation (15), and it does not occur too deep in the CSM, since the latter is not very dense.

Figure 3 shows the muon neutrino fluence expected from AT2018cow and CSS161010. The blue band corresponds to the neutrino fluence from the choked jet, while the orange and purple bands represent the neutrino signal from CSM interaction in the cocoon and merger models, respectively. Each band reflects the uncertainties on the model parameters discussed in Section 3 (see Table 1). The neutrino fluence for the choked jet scenario is displayed for the optimistic case of a jet observed on axis. If the jet axis should be perpendicular with respect to the line of sight of the observer, no neutrino is expected. In the following, we assume that the choked jet points toward the observer; this might have been the case for AT2018cow, because two neutrinos have been detected at IceCube in its direction (Blaufuss 2018; Stein 2021)—see the discussion below. On the other hand, the emission from CSM interaction is approximately isotropic and hence observable from any viewing angle. This is consistent with electromagnetic observations of LFBOTs: if a choked jet is harbored, no electromagnetic emission is expected. The optical radiation is powered from the cooling of the cocoon, while the radio emission comes from the interaction of the cocoon with the CSM (Gottlieb et al. 2022b). In the merger model, the fast outflow responsible for the high-energy neutrino emission likely covers about $\gtrsim$70% of the solid angle 4π (Metzger 2022); hence, its emission is quasi-isotropic and visible from along any observer direction.

Both for the cocoon and merger models, CSM interaction produces a smaller neutrino fluence than in the case of the choked jet model. Nevertheless, the merger model allows for a larger neutrino fluence compared to the cocoon one. This result is justified in the light of the larger CSM densities. Even though the stellar mass-loss rates are comparable, the wind speed is lower in the merger model than in the cocoon model (10 and 1000 km s^{-1}, respectively; in the former model, it is generated by mass loss from the disk, while it is due to mass loss from the progenitor star prior to its explosion in the latter model). If a choked jet is harbored in LFBOTs and points toward the observer, then it dominates the neutrino emission. The neutrino emission from the choked jet model is in qualitative agreement with Murase & Ioka (2013); He et al. (2018); Senno et al. (2016), which focused on forecasting the neutrino production in gamma-ray bursts instead. Our results concerning the

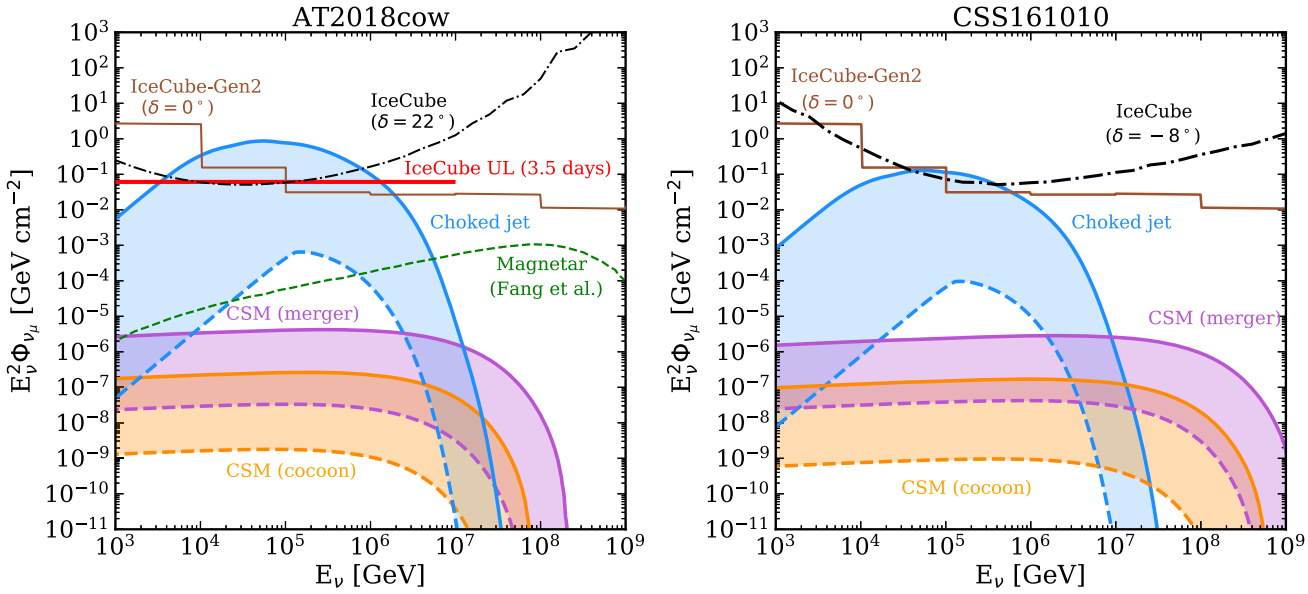

Figure 3. Muon neutrino fluence expected from AT2018cow (left panel, $z = 0.0141$, $\delta = 22°$) and CSS161010 (right panel, $z = 0.034$, $\delta = -8°$). The blue shaded region corresponds to the contribution to the neutrino signal from the choked jet, while the orange (purple) shaded region displays the signal from interaction between the CSM and the fast component of the outflow in the cocoon (merger) model. The continuous (dashed) lines are the upper (lower) limits on the neutrino fluence, corresponding to the ranges of parameter values listed in Table 1. The neutrino emission from the choked jet scenario is strongly dependent on the direction, while the one from the CSM scenarios is quasi-isotropic. The neutrino fluence in the choked jet scenario is shown in the most optimistic case of a jet oriented along the line of sight of the observer. For comparison, we show the results of Fang et al. (2019; green dashed line), corresponding to the neutrino fluence in the event that a magnetar powers AT2018cow. The sensitivity of IceCube for point sources is plotted at a decl. $\delta = 22°$ and $\delta = -8°$ (Aartsen et al. 2014; black dotted–dashed lines), as measured for AT2018cow and CSS161010, respectively. The sensitivity of IceCube-Gen2 to a point source at $\delta = 0°$ is also shown (sienna line). The neutrino fluence from the choked jet harbored in LFBOTs—if the jet points toward the observer—is comparable with the sensitivities of IceCube and IceCube-Gen2. For AT2018cow, we show the upper limit set by IceCube on the time-integrated ν_μ fluence (IceCube UL, red line), corresponding to the observation of two neutrino events in coincidence with AT2018cow (Blaufuss 2018; Stein 2021).

neutrino signal from ejecta–CSM interaction are valid for every model invoking the emission of a fast outflow propagating outwards in the CSM. On the contrary, the neutrino emission from the choked jet is model dependent. Recent numerical simulations show that efficient acceleration in jets can occur if the jet is weakly or mildly magnetized (Gottlieb & Globus 2021); if this should be the case for LFBOTs, a dedicated investigation of the neutrino production in this scenario would be required. Furthermore, we have calculated the neutrino signal from the jet assuming that it is choked in the extended stellar envelope. As discussed in Section 3 and shown in Figure 2, a choked jet may be harbored only for certain pairs of the jet luminosity and lifetime.

For comparison, in Figure 3, we show the sensitivity of IceCube for point sources at the decl. $\delta = 22°$ (for AT2018cow) and $\delta = -8°$ (for CSS161010; Aartsen et al. 2014) and the projected sensitivity of IceCube-Gen2 for a point-like source at $\delta = 0°$ (Aartsen et al. 2021). If a source similar to AT2018cow (or CSS161010) were to be observed in the future at this decl. by IceCube-Gen2, the detection chances of neutrinos from the choked jet scenario would be comparable to the ones of IceCube. This is mainly due to the fact that the sensitivity of IceCube-Gen2 will be better than the one of IceCube in the PeV–EeV energy range but comparable at lower energies; the fluence from the choked jet peaks in the TeV–PeV range. As for the CSM interaction, the neutrino fluence lies well below the sensitivity curve of both IceCube and IceCube-Gen2.

Other neutrino detectors are planned to be operative in the future, such as GRAND 200k (Álvarez-Muñiz et al. 2020), RNO–G (Aguilar et al. 2021), and POEMMA (Olinto et al. 2021). These neutrino telescopes aim to probe ultrahigh-energy neutrinos, but their sensitivity in the PeV–EeV energy range is worse than the one of IceCube-Gen2; therefore we do not show them in Figure 3.

In Figure 3, we plot the upper limit set by IceCube on the muon neutrino fluence for AT2018cow. This upper limit corresponds to the observation of two IceCube neutrino events in coincidence with AT2018cow at 1.8σ confidence level within a time window of 3.5 days after the optical discovery (Blaufuss 2018; Stein 2021). The envelope obtained for AT2018cow overshoots this limit for $\tilde{E}_j^{\rm iso} \gtrsim 10^{52}$ erg. Interestingly, $\tilde{E}_j^{\rm iso} \gtrsim 10^{52}$ erg falls in the range inferred by electromagnetic observations; see Table 1. This finding intriguingly suggests that the existing neutrino data may further restrict the allowed parameter space shown in Figure 2 for AT2018cow, as displayed in Figure 4. No neutrino search has been performed in the direction of CSS161010 instead.

As discussed in Section 3, the CO of LFBOTs could be a magnetar. In this case, high-energy neutrinos could be produced in the proximity of the magnetar (Murase et al. 2009; Fang et al. 2014; Fang & Metzger 2017). Protons (or other heavier nuclei) may be accelerated in the magnetosphere and then interact with photons and baryons in the ejecta shell surrounding the CO. Both $p\gamma$ and pp interactions can efficiently produce neutrinos in the PeV–EeV energy band. The neutrino production from a millisecond magnetar has been investigated in Fang et al. (2020) for AT2018cow. We show the expected muon neutrino fluence at Earth obtained in Fang et al. (2020) in Figure 3 for comparison with the other scenarios explored in this paper. For CSS161010, we expect a neutrino fluence qualitatively similar to the one considered for AT2018cow.

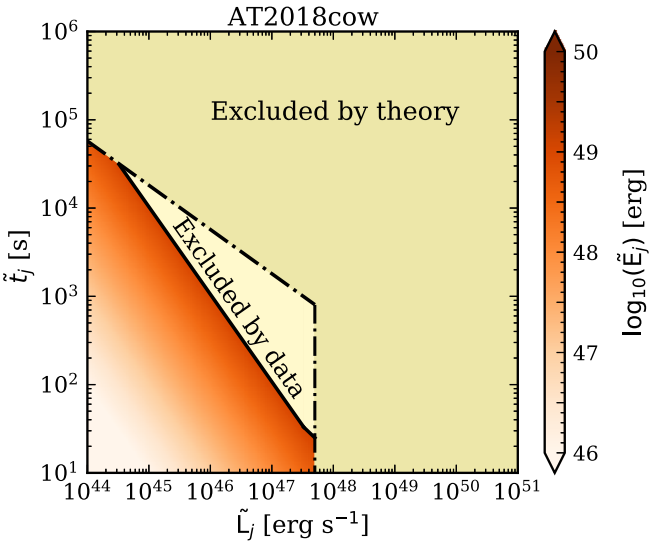

Figure 4. Contour plot of the jet energy $\tilde{E}_j$ in the parameter space spanned by $(\tilde{L}_j, \tilde{t}_j)$ for AT2018cow and $\Gamma = 100$. Part of the parameter space allowed in Figure 2 is excluded by the IceCube neutrino data (light-yellow region), since the correspondent neutrino emission would overshoot the upper limit set by IceCube on the time-integrated ν_μ flux from for AT2018cow (Blaufuss 2018; Stein 2021). Another portion of the parameter space (dark yellow region) is excluded by theoretical arguments, as already shown in Figure 2. For $\Gamma = 10$, the region of the parameter space excluded by the IceCube data is smaller and overlaps with the one excluded by theory. The region of the parameter space excluded by the IceCube data is obtained under the assumption of an on-axis choked jet; see discussion in the main text.

If a magnetar is the central engine of LFBOTs, its contribution to the neutrino fluence would be relevant in the PeV–EeV band, at energies higher than the typical ones for neutrino emission from the choked jet and CSM interaction. Note that the comparison between the fluence from the magnetar and our results is consistent as for the energetics of the CO. Indeed, the set of parameters adopted by Fang et al. (2019) leads to $\tilde{E} \simeq 10^{50}$–10^{51} erg injected by the magnetar in its spin-down time, $\tilde{t}_{\rm sd} \simeq 8.4 \times 10^3$–$8.4 \times 10^4$ s. If a jet is launched by the magnetar, then these quantities correspond to its energy and its lifetime, consistently with the ranges we are exploring in our work.

The radio extension of IceCube-Gen2 (Aartsen et al. 2021), as well as the neutrino facilities GRAND200k (Álvarez-Muñiz et al. 2020), POEMMA (Olinto et al. 2021), and RNO–G (Aguilar et al. 2021), will be more sensitive than IceCube (Aartsen et al. 2021) for what concerns the emission of neutrinos in the magnetar scenario, and they may detect neutrinos from sources similar to AT2018cow, occurring at a smaller distance.

5.2. Neutrino Event Rate

Given the muon neutrino fluence up to the time t, $\Phi_{\nu_\mu}(E_\nu, t)$, the cumulative number of muon neutrinos expected at IceCube up to the same time is

$$N_{\nu_\mu}(t) = \int_{E_{\nu,\rm min}}^{E_{\nu,\rm max}} dE_\nu \Phi_{\nu_\mu}(E_\nu, t) A_{\rm eff}(E_\nu, \delta), \quad (33)$$

where $E_{\nu,\rm min} = 10^2$ GeV and $E_{\nu,\rm max} = 10^{10}$ GeV are the minimum and maximum neutrino energies, respectively, and $A_{\rm eff}(E_\nu, \delta)$ is the effective area as a function of energy and for a fixed source decl. δ (Abbasi et al. 2021b). The background of atmospheric muon neutrinos can be estimated by following Razzaque & Yang (2015):

$$N_{\nu_\mu,\rm back}(t) = \pi \Delta\delta^2 \int_{E_{\nu,\rm min}}^{E_{\nu,\rm max}} dE_\nu A_{\rm eff}(E_\nu, \delta) \Phi_{\nu_\mu}^{\rm atm}(E_\nu, \theta, t), \quad (34)$$

where $\Phi_{\nu_\mu}^{\rm atm}(E_\nu, \theta, t)$ is the fluence of atmospheric neutrinos at the time t, from the zenith angle θ, and $\Delta\delta \simeq 2^\circ.5$ is the width of the angular interval within which is defined the effective area $A_{\rm eff}(E_\nu, \delta)$ of IceCube. For IceCube, the relation $\theta = 90^\circ + \delta$ holds (Aartsen et al. 2017). We compute the atmospheric background by using the model presented in Stanev (2010); Gaisser & Honda (2002); Gaisser (2019).

We show the cumulative number of neutrinos from the choked jet scenario (for a jet pointing toward the observer) and CSM interaction (both for the cocoon and merger models) as functions of time both for AT2018cow and CSS161010 in Figure 5. Note that, for AT2018cow, the upper limit of the choked jet scenario is calculated by assuming $\tilde{E}_j^{\rm iso} = 10^{51}$ erg, in agreement with the allowed region of the parameter space shown in Figure 4. The upper and lower limits for the cumulative number of neutrinos in the CSM interaction models for AT2018cow and for all the scenarios considered for CSS161010 are the same as the ones in Table 1. The thick lines denote the duration of the signal, which can last up to a few months for CSM interaction. As for the choked jet, the neutrino rate is expected to be constant during the jet lifetime, in the simple approximation that N internal shocks occur in the jet during this period, and each of them produces the same neutrino signal. Hence, the cumulative neutrino rate from the choked jet grows linearly with time up to the jet lifetime. For CSM interaction, the number of neutrinos rapidly increases after the breakout and then reaches a plateau since the proton injection is balanced by pp energy losses. The atmospheric background neutrinos increase linearly with time. The background is expected to dominate over the signal from CSM interaction, both for the cocoon and merger models; on the contrary, the background becomes comparable to the choked jet signal at times larger than the jet lifetime.

5.3. Detection Prospects for AT2018cow and CSS161010

The neutrino signal from LFBOTs overlaps in energy with the atmospheric neutrino background. In order to gauge the possibility of discriminating the LFBOT signal from the one of atmospheric neutrinos, we compare the total number of muon neutrinos of astrophysical origin $N_{\nu_\mu,\rm astro}$ with the total number of background atmospheric neutrinos $N_{\nu_\mu,\rm back}$. The former is given by the sum between the contributions from the choked jet and CSM interaction in the cocoon model and by CSM interaction only in the merger model. Each contribution is computed by relying on Equation (33) and integrating over the duration of the neutrino production, defined for each case in Section 4.3. The latter is obtained through Equation (34), during the duration of neutrino production for each model.

Below 100 TeV, the astrophysical neutrino events need to be carefully discriminated against the atmospheric ones. Hence, we consider two scenarios: a conservative energy cutoff in Equation (33), $E_{\nu,\rm min} = 100$ TeV (corresponding to the case when the atmospheric neutrino events cannot be distinguished

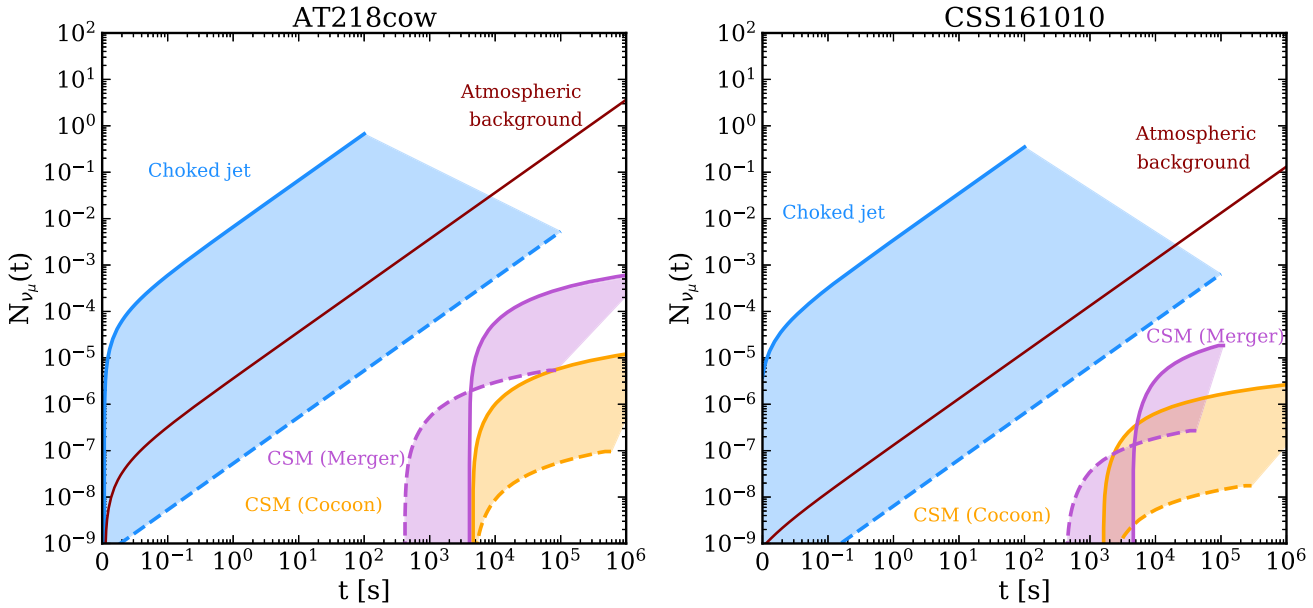

Figure 5. Cumulative number of muon neutrinos for AT2018cow (left panel) and CSS161010 (right panel) expected at the IceCube Neutrino Observatory; see Table 1. The blue shaded region corresponds to the contribution from the choked jet (when the latter is observed on axis); the orange (purple) shaded region corresponds to neutrinos from CSM interaction in the cocoon (merger) model. The rate of neutrinos from the choked jet is expected to be constant in the approximation that N internal shocks occur in the jet during its lifetime and that each of them produces the same neutrino signal. Therefore, the neutrino signal grows linearly with time up to the end of the jet lifetime. For CSM interaction, the number of neutrinos rapidly increases and settles to a constant value because the proton injection is balanced by pp energy losses. The upper and lower limits of each band correspond to the same uncertainty ranges in Table 1 and Figure 3, except for the upper limit for the choked jet scenario in AT2018cow for which we take $\tilde{E}_j^{\rm iso} = 10^{51}$ erg, consistently with the IceCube constraints—see Figure 4. The brown line shows the cumulative number of atmospheric neutrinos (which constitutes a background for the detection of astrophysical neutrinos), which increases linearly with time.

Table 2
Total Number of Astrophysical Neutrinos ($N_{\nu_\mu,\rm astro}$) and Atmospheric Neutrinos ($N_{\nu_\mu,\rm back}$) in the Cocoon (Including Choked Jet and CSM Interaction) and Merger Models, for $E_{\nu,\rm min} = 100$ TeV

N_{ν_μ}	AT2018cow	CSS161010
	Cocoon Model	
$N_{\nu_\mu,\rm astro}$	3×10^{-3}–0.15 ($7\times10^{-3}-0.67$)	3×10^{-4}–0.23 ($4\times10^{-4}-0.35$)
$N_{\nu_\mu,\rm back}$	$9\times10^{-4}-3\times10^{-3}$ (2.23 − 9.71)	$5\times10^{-4}-1.4\times10^{-2}$ ($2.6\times10^{-2}-0.64$)
	Merger Model	
$N_{\nu_\mu,\rm astro}$	1.5×10^{-6}–2.1×10^{-4} ($1.5\times10^{-6}-2\times10^{-4}$)	6.5×10^{-7}–4.5×10^{-5} ($8\times10^{-7}-5\times10^{-5}$)
$N_{\nu_\mu,\rm back}$	$1\times10^{-4}-3\times10^{-3}$ (0.32 − 8)	$8\times10^{-5}-2\times10^{-3}$ ($3.7\times10^{-3}-9.2\times10^{-2}$)

Note. The correspondent neutrino numbers obtained by adopting $E_{\nu,\rm min} = 100$ GeV are displayed in parenthesis. The range of variability corresponds to the upper and lower limits shown in Figure 5.

from the astrophysical ones below 100 TeV) and a low energy cutoff, $E_{\nu,\rm min} = 100$ GeV (representative of the instance of full discrimination of the events of astrophysical origin).

Our results are summarized in Table 2. The number of astrophysical neutrinos expected in the cocoon model is larger than the number of atmospheric neutrinos, both for AT2018cow and CSS161010, when the energy cutoff $E_{\nu,\rm min} = 100$ TeV is adopted. Hence, the detection chances of the astrophysical neutrinos above 100 TeV may be promising, if a choked jet pointing toward the observer is harbored in LFBOTs. The number of astrophysical neutrinos may instead be smaller than or comparable to the atmospheric background for the merger model; therefore, the background signal cannot be fully discriminated; this is especially evident for $E_{\nu,\rm min} = 100$ GeV.

In the event of detection of one or a few neutrinos from LFBOTs and depending on the number of undetected sources from the LFBOT population, the actual neutrino flux could be smaller than the one estimated by relying on the detected events. For this reason, we need to correct for the Eddington bias on neutrino observations (Strotjohann et al. 2019). Assuming that the local rate of LFBOTs is $\sim 0.4\%$ of the core-collapse SN rate (Coppejans et al. 2020), we consider the effective density integrated over the cosmic history of LFBOTs to be $\mathcal{O}(10^4)$ Mpc^{-3}. The latter has been computed by assuming the density of core-collapse SNe equal to 1.07×10^7 Mpc^{-3} (Yuksel et al. 2008; Vitagliano et al. 2020) and the redshift evolution of LFBOTs identical to the one of the star formation rate. After taking into account these inputs, from Figure 2 of Strotjohann et al. (2019), we find that the number of expected events in Table 2 could be compatible with the

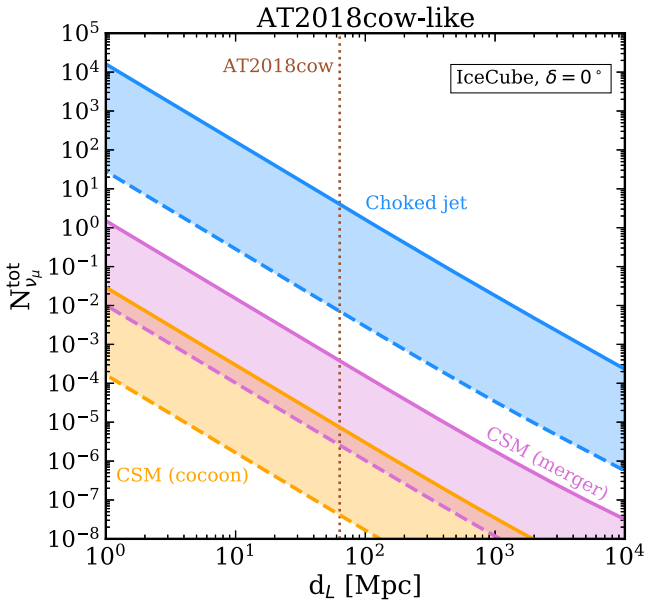

Figure 6. Total number of muon neutrinos expected at the IceCube Neutrino Observatory as a function of the luminosity distance for an AT2018cow-like source from the choked jet pointing toward the observer (blue shaded region) and CSM interaction in the cocoon and merger models (orange and purple shaded regions, respectively). The bands are obtained by adopting the parameter uncertainty ranges listed in Table 1 for AT2018cow. The source is placed at $\delta = 0°$. The brown vertical line marks the distance of AT2018cow to guide the eye. The number of neutrinos decreases as a function of the luminosity distance, as expected.

observation of 1–3 neutrino events both from AT2018cow and CSS161010.

The IceCube Neutrino Observatory reported the detection of two track-like neutrino events in the direction of AT2018cow compatible with the expected number of atmospheric neutrino events (Blaufuss 2018). Our findings hint that the observation of two neutrino events may also be compatible with the expected number of neutrinos of astrophysical origin. A dedicated neutrino search in the direction of CSS161010, during the time when the transient was electromagnetically bright, would be desiderable.

5.4. Future Detection Prospects

The rate of LFBOTs and its redshift dependence are still very uncertain. In order to forecast the detection prospects in neutrinos for upcoming LFBOTs, we consider a LFBOT with properties similar to the ones of AT2018cow (see Table 1). Figure 6 shows the total number of neutrinos expected at the IceCube Neutrino Observatory in the choked jet scenario and for CSM interaction (both in the cocoon and merger models) as functions of the luminosity distance of the AT2018cow-like source; of course, similar conclusions would hold for a LFBOT resembling the CSS161010 source; see Figures 3 and 5. We assume the upper and lower limits for AT2018cow listed in Table 1, because the neutrino constraints shown in Figure 4 do not hold for this source. We assume that the source is at $\delta = 0°$, in order to guarantee the maximal effective area at IceCube (Abbasi et al. 2021b), and perform the integral in Equation (33) between the initial (t_i) and final (t_f) times of neutrino production as described in Section 4.3. Furthermore, we adopt the conservative lower energy cutoff $E_{\nu,\min} = 100$ TeV, in order to better discriminate the neutrinos of astrophysical origin from atmospheric background neutrinos.

Figure 6 shows that the number of neutrinos expected in the choked jet scenario for an AT2018cow-like source located at $1\ \mathrm{Mpc} \lesssim d_L \lesssim 10^4$ Mpc is $10^{-6} \lesssim N_{\nu_\mu}^{\rm tot} \lesssim 10^4$ if the jet points toward the observer. As for CSM interaction, the number of expected neutrinos for the same source located at $1\ \mathrm{Mpc} \lesssim d_L \lesssim 10^4$ Mpc for the cocoon model (merger model) is $2 \times 10^{-12} \lesssim N_{\nu_\mu}^{\rm tot} \lesssim 3 \times 10^{-2}$ $(10^{-10} \lesssim N_{\nu_\mu}^{\rm tot} \lesssim 2)$. We expect comparable or better detection chances for IceCube-Gen2 (see Figure 3). We stress that a detailed statistical analysis may provide improved detection prospects, but this is out of the scope of this work. Nevertheless, our results are an intriguing guideline for upcoming follow-up neutrino searches of LFBOTs.

6. Diffuse Neutrino Emission

Despite the growing number of neutrino events routinely detected at IceCube, the origin of the observed diffuse neutrino background is still unknown. Several source classes have been proposed as major contributors to the observed diffuse flux, such as gamma-ray bursts, cluster of galaxies, star-forming galaxies, tidal disruption events, and SNe (Mészáros 2017a; Ahlers & Halzen 2018; Vitagliano et al. 2020; Mészáros 2017b; Pitik et al. 2021; Murase 2017; Waxman 2017; Tamborra et al. 2014; Zandanel et al. 2015; Wang & Liu 2016; Dai & Fang 2017; Senno et al. 2017; Lunardini & Winter 2016; Sarmah et al. 2022). As discussed in Section 5, LFBOTs have favorable detection chances in neutrinos; hence we now explore the contribution of LFBOTs to the diffuse neutrino background.

The diffuse neutrino background is

$$F_\nu^{\rm back} = \frac{c}{4\pi H_0} \int_0^{z_{\max}} dz \frac{f_b R_{\rm SFR}(z)}{\sqrt{\Omega_M (1+z)^3 + \Omega_\Lambda}} \phi_\nu(E'_\nu), \quad (35)$$

where $z_{\max} = 8$, $\phi_\nu(E'_\nu)$ is the differential neutrino number from a single burst (in units of GeV^{-1}; defined multiplying Equation (32) by the luminosity distance), $E'_\nu = E_\nu(1+z)/\Gamma$ (where $\Gamma = 1$ for CSM interaction). The beaming factor is given by $f_b = \Omega/4\pi \simeq \theta_j^2/2$ for the choked jet, while $f_b = 1$ for CSM interaction. The factor takes into account the beaming of the jet within an opening angle θ_j. The beaming is not relevant in *pp* interactions, because they originate from the cocoon (or the polar fast outflow) whose opening angle is wider than the one of the jet (Gottlieb et al. 2022a). Therefore, the geometry of the outflow can be assumed to be spherical.

So far, the luminosity function for LFBOTs is not available because only a few transients have been identified as belonging to this emerging class. Thus, we fix the isotropic equivalent energy of the choked jet $\tilde{E}_j^{\rm iso} = 10^{51}$ erg, its Lorentz factor $\Gamma = 100$, and we assume that it is representative of the whole population. For computing the contribution to the diffuse neutrino background from CSM interaction, we assume $M_{\rm ej} = 10^{-2} M_\odot$, $\dot{M} = 10^{-3} M_\odot\ \mathrm{yr}^{-1}$, $v_{\rm w} = 1000\ \mathrm{km\ s}^{-1}$, and $v_{\rm sh} = 0.3c$ as representative values.

We assume that the redshift evolution of LFBOTs follows the star formation rate, $R_{\rm SFR}(z)$ (Yuksel et al. 2008):

$$R_{\rm SFR}(z) = R_{\rm FBOT}(z=0) \times \left[(1+z)^{-34} + \left(\frac{1+z}{5000}\right)^{-3} + \left(\frac{1+z}{9}\right)^{-35}\right] \quad (36)$$

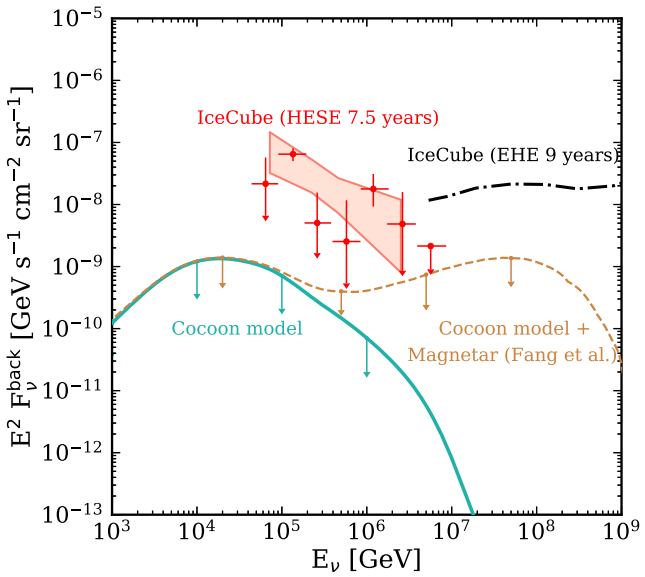

Figure 7. Upper limit on the all-flavor diffuse neutrino flux from LFBOTs obtained by including the contribution from a choked jet and CSM interaction (cocoon model; sea green solid line) as a function of the neutrino energy. We show the cocoon model only, since it includes both the choked jet and CSM interaction; the merger model would give rise to a diffuse flux lying well below the sea green line. For comparison, the upper limit obtained including both the cocoon model and the contribution from the magnetar (taken from Fang et al. 2019) is also shown (light-brown dashed line). The pink band corresponds to the fit to the 7.5 yr IceCube high-energy starting events (HESE), plotted as red data points (Abbasi et al. 2021c). The black dotted–dashed line corresponds to the 9 yr extreme-high-energy (EHE) 90% upper limit set by the IceCube Neutrino Observatory (Aartsen et al. 2018b). The diffuse neutrino background from LFBOTs lies below IceCube data.

where the local rate of LFBOTs is assumed to be $R_{\rm FBOT}(z=0) \lesssim 300$ Gpc^{-3} yr^{-1} (Coppejans et al. 2020; Ho et al. 2021).

Figure 7 shows the upper limit to the diffuse neutrino background resulting from the choked jet and CSM interaction (cocoon model; sea green solid line). For comparison, we also show the upper limit on the total diffuse emission when we include the contribution from a millisecond magnetar, i.e., when we sum up the diffuse emission from choked jet, CSM interaction, and the magnetar itself (light-brown dashed line). The diffuse emission from the magnetar only has been taken from Fang et al. (2019), and it has been rescaled to the local rate assumed in this paper, referring to the subclass of LFBOTs. Note that here we consider the cocoon model only, since it includes both a choked jet and CSM interaction, and thus it would lead to the most optimistic estimation of the expected neutrino background. If the merger model is adopted, the resulting diffuse neutrino background is flat at low energies, with an energy cutoff around 10^7 GeV; hence, the merger model would give rise to a diffuse emission below the sea green line in Figure 7 and consistent with the upper limit we are showing.

We compare our results with the flux constraints from the 7.5 yr high-energy starting event data set (HESE 7.5 yr; Abbasi et al. 2021c) and the 9 yr extreme-high-energy (EHE) 90% upper limit set by the IceCube Neutrino Observatory (Aartsen et al. 2018b) in Figure 7. Our results suggest that LFBOTs do not constitute the bulk of the diffuse neutrino flux detected by the IceCube Neutrino Observatory. Nevertheless, the typical energies of these objects might be larger that the ones assumed in this work, resulting in a larger diffuse neutrino emission.

7. Conclusions

Despite the growing number of observations of LFBOTs, their nature remains elusive. Multimessenger observations could be crucial to gain insight on the source engine.

In this paper, we consider the scenarios proposed in Gottlieb et al. (2022b; cocoon model) and Metzger (2022; merger model) for powering LFBOTs and aiming to fit the multi-wavelength electromagnetic observations and mounting evidence for asymmetric LFBOT outflows. In the cocoon model, neutrinos could be produced in the jet choked within the extended envelope of the collapsing massive star. The existence of a jet harbored in LFOBTs is highly uncertain, and certain conditions on its luminosity and lifetime must be satisfied for the jet to be choked. If a jet is launched by the CO and choked, it contributes to inflate the cocoon; the latter breaks out of the stellar envelope and interacts with the CSM; neutrinos could also be produced at the collisionless shocks occurring at the interface between the cocoon and the CSM. In the merger model, a black hole surrounded by an accretion disk forms as a result of the merger of a Wolf–Rayet star with a black hole. The disk outflow in the polar region propagates in the CSM, possibly giving rise to neutrino production.

By using the model parameters inferred from the electromagnetic observations of two among the most studied LFBOTs, AT2018cow and CSS161010, we find that the neutrinos with energies up to $\mathcal{O}(10^9)$ GeV could be produced in the cocoon and merger models. The neutrino signal from the choked jet would be detectable only if the observer line of sight is located within the opening angle of the jet. If this is the case, the upper limit on the neutrino emission set by the IceCube Neutrino Telescope on AT2018cow (Blaufuss 2018) already allows us to exclude a region of the FBOT parameter space, otherwise compatible with electromagnetic observations. On the contrary, the existence of a fast outflow ($v_{\rm ej} \gtrsim 0.1$ c) interacting with the CSM is supported by electromagnetic observations. The results concerning the neutrino signal from CSM interaction are therefore robust and valid for any viewing angle of the observer, being the emission isotropic in good approximation.

We find that the neutrino emission from LFBOTs does not account for the bulk of the diffuse neutrino background observed by IceCube. Nevertheless, the neutrino fluence from a single LFBOT is especially large in the choked jet scenario, if the jet should be observed on axis, and is comparable to the sensitivity of the IceCube Neutrino Observatory and IceCube-Gen2, while it is below the IceCube sensitivity for the CSM interaction cases.

By taking into account the Eddington bias on the observation of cosmic neutrinos, we conclude that the two track-like events observed by IceCube in coincidence with AT2018cow may have been of astrophysical origin (similar conclusions would hold for CSS161010). In the light of these findings, a search for neutrino events in coincidence with the other known LFBOTs should be carried out.

In conclusion, the detection of the neutrinos from LFBOTs with existing and upcoming neutrino telescopes will be crucial to probe the mechanism powering FBOTs. The choked jet and CSM interaction would generate very different neutrino signals: the former is direction dependent and peaks around

$E_\nu \simeq 10^5$ GeV; the latter is quasi-isotropic and approximately flat up to $E_\nu \simeq 10^7$–10^8 GeV for our fiducial parameters. Current neutrino telescopes may not be able to clearly differentiate the signals from the choked jet and CSM interaction scenarios. Nevertheless, CSM interaction can produce neutrinos in the high-energy tail of the spectrum, e.g., the detection of neutrinos with energies of $\mathcal{O}(100)$ PeV may hint toward the CSM interaction origin; on the other hand, if a choked jet is harbored in LFBOTs and the jet is observed on axis, a large number of neutrinos with $\mathcal{O}(100)$ TeV energy is expected to be detected at IceCube and IceCube-Gen2. As the number of detected LFBOTs increases, neutrino searches have the potential to provide complementary information on the physics of these emergent transient class and their rate.

We thank Erik Blaufuss for useful discussions as well as Ore Gottlieb and Brian Metzger for insightful comments on the manuscript. This project has received funding from the Villum Foundation (Project No. 37358), the Carlsberg Foundation (CF18-0183), the Deutsche Forschungsgemeinschaft through Sonderforschungsbereich SFB 1258 "Neutrinos and Dark Matter in Astro- and Particle Physics" (NDM), and the National Science Foundation under award Nos. AST-1909796 and AST-1944985.

Appendix
Proton and Meson Cooling Times

For the choked jet case, the acceleration timescale of protons is

$$t'^{-1}_{\rm acc} = \frac{ceB'}{\xi E'_p}, \tag{A1}$$

where $e = \sqrt{\hbar\alpha c}$ is the electric charge with $\alpha = 1/137$ being the fine structure constant, and $\hbar$ is the reduced Planck constant. ξ defines the number of gyroradii needed for accelerating protons, and we assume $\xi = 10$ (Gao et al. 2012). Finally, B' is the magnetic field generated at the internal shock; see main text.

For CSM interaction, the acceleration timescale is obtained in the Bohm limit (Protheroe & Clay 2004)

$$t'^{-1}_{\rm acc} \simeq \frac{3eB'v_{\rm sh}^2}{20\gamma_p m_p c^3}, \tag{A2}$$

where $B' \equiv \tilde{B}$ is the magnetic field in the shocked interacting shell; see main text.

Protons accelerated at the shocks undergo several energy loss processes. The total cooling time is

$$t'^{-1}_{p,\rm cool} = t'^{-1}_{\rm ad} + t'^{-1}_{p,\rm sync} + t'^{-1}_{p\gamma} + t'^{-1}_{pp} + t'^{-1}_{p,\rm BH} + t'^{-1}_{p,\rm IC}, \tag{A3}$$

where $t'^{-1}_{\rm ad}$, $t'^{-1}_{p,\rm sync}$, $t'^{-1}_{p\gamma}$, t'^{-1}_{pp}, $t'^{-1}_{p,\rm BH}$, $t'^{-1}_{p,\rm IC}$ are the adiabatic, synchrotron, photohadronic ($p\gamma$), hadronic (pp), Bethe–Heitler (BH, $p\gamma \to pe^+e^-$), and inverse Compton cooling timescales, respectively. These are defined as follows (Dermer & Menon 2009; Gao et al. 2012; Razzaque et al. 2005):

$$t'^{-1}_{\rm ad} = \frac{v}{R}, \tag{A4}$$

$$t'^{-1}_{p,\rm sync} = \frac{4\sigma_T m_e^2 E'_p B'^2}{3m_p^4 c^3 8\pi}, \tag{A5}$$

$$t'^{-1}_{p\gamma} = \frac{c}{2\gamma'^2_p}\int_{E_{\rm th}}^{\infty} dE'_\gamma \frac{n'_\gamma(E'_\gamma)}{E'^2_\gamma}\int_{E_{\rm th}}^{2\gamma'_p E'_\gamma} dE_r E_r \sigma_{p\gamma}(E_r) K_{p\gamma}(E_r), \tag{A6}$$

$$t'^{-1}_{pp} = cn'_p \sigma_{pp} K_{pp}, \tag{A7}$$

$$t'^{-1}_{p,\rm BH} = \frac{7m_e\alpha\sigma_T c}{9\sqrt{2}\pi m_p \gamma'^2_p}\int_{\gamma'^{-1}_p}^{\frac{E'_{\gamma,\rm max}}{m_e c^2}} d\epsilon' \frac{n'_\gamma(\epsilon')}{\epsilon'^2} \times \left\{(2\gamma'_p\epsilon')^{3/2}\left[\ln(\gamma'_p\epsilon') - \frac{2}{3}\right] + \frac{2^{5/2}}{3}\right\}, \tag{A8}$$

$$t'^{-1}_{p,\rm IC} = \frac{3(m_e c^2)^2\sigma_T c}{16\gamma'^2_p(\gamma'_p - 1)\beta'_p}\int_{E'_{\gamma,\rm min}}^{E'_{\gamma,\rm max}} \frac{dE'_\gamma}{E'^2_\gamma} F(E'_\gamma, \gamma'_p) n'_\gamma(E'_\gamma), \tag{A9}$$

where $v = 2c\Gamma$ for the choked jet and $v = v_{\rm sh}$ for CSM interactions; $\gamma_p = E'_p/m_p c^2$, $\epsilon' = E'_\gamma/m_e c^2$, $E_{\rm th} = 0.150$ GeV is the energy threshold for photopion production, and $\beta'_p \approx 1$ for relativistic particles. The function $F(E'_\gamma, \gamma'_p)$ follows the definition provided in Jones (1965), replacing $m_e \to m_p$. The cross sections for $p\gamma$ and pp interactions, $\sigma_{p\gamma}$ and σ_{pp}, can be found in Zyla et al. (2020). The function $K_{p\gamma}(E_r)$ is the $p\gamma$ inelasticity, given by Equation (9.9) of Dermer & Menon (2009):

$$K_{p\gamma}(E_r) = \begin{cases} 0.2 & E_{\rm th} < E_r < 1\ {\rm GeV} \\ 0.6 & E_r > 1\ {\rm GeV} \end{cases} \tag{A10}$$

where $E_r = \gamma'_p E'_\gamma(1 - \beta'_p \cos\theta')$ is the relative energy between a proton with Lorentz factor γ'_p and a photon with energy E'_γ, whose directions form an angle θ' in the comoving frame of the interaction region. The comoving proton density is $n'_p = 4\tilde{L}_j/(4\pi R_{\rm IS}^2 c m_p c^3 \theta_j^2)$ for the choked jet, and $n'_p = \tilde{n}_p = 4n_{p,\rm CSM} m_p c^2$ for CSM interaction. The inelasticity of pp interactions is $K_{pp} = 0.5$, and $n'_\gamma(E'_\gamma)$ is the photon target for accelerated protons.

At the internal shock, the secondary charged mesons undergo energy losses before decaying; in turn, affecting the neutrino spectrum. In Figure 8, we show an example obtained for $\tilde{L}_j = 2 \times 10^{47}$ erg s^{-1}, $\tilde{t}_j = 20$ s, and $\Gamma = 100$. We note that, in the choked jet, $p\gamma$ interactions are the main energy loss channel for protons, while secondaries mainly cool through adiabatic losses. Kaons cool at an energy much higher than the maximum proton energy; therefore their cooling does not affect the neutrino spectrum (He et al. 2012; Asano & Nagataki 2006; Petropoulou et al. 2014; Tamborra & Ando 2015).

As for CSM interaction, the only relevant cooling processes for protons are hadronic cooling (pp interactions) and adiabatic cooling. The photons produced at the external shock between the ejecta and the CSM have energies in the radio band, i.e., at low energies. Therefore the interactions between protons and photons are negligible, consistently with Murase et al. (2011); Fang et al. (2020). For CSM interaction, $t'^{-1}_{\rm cool} = t'^{-1}_{pp} + t'^{-1}_{\rm ad}$ (note that since shocks are nonrelativistic, there is no difference between the comoving frame of the shock and the CO frame for CSM interaction). The proton cooling times are shown at $R_{\rm bo}$ and $10R_{\rm bo}$ in Figure 9 for $v_{\rm ej} = 0.55c$, $M_{\rm ej} = 3.7 \times 10^{-2} M_\odot$, and $M_{\rm CSM} = 10^{-1} M_\odot$. We note that the pp interactions are

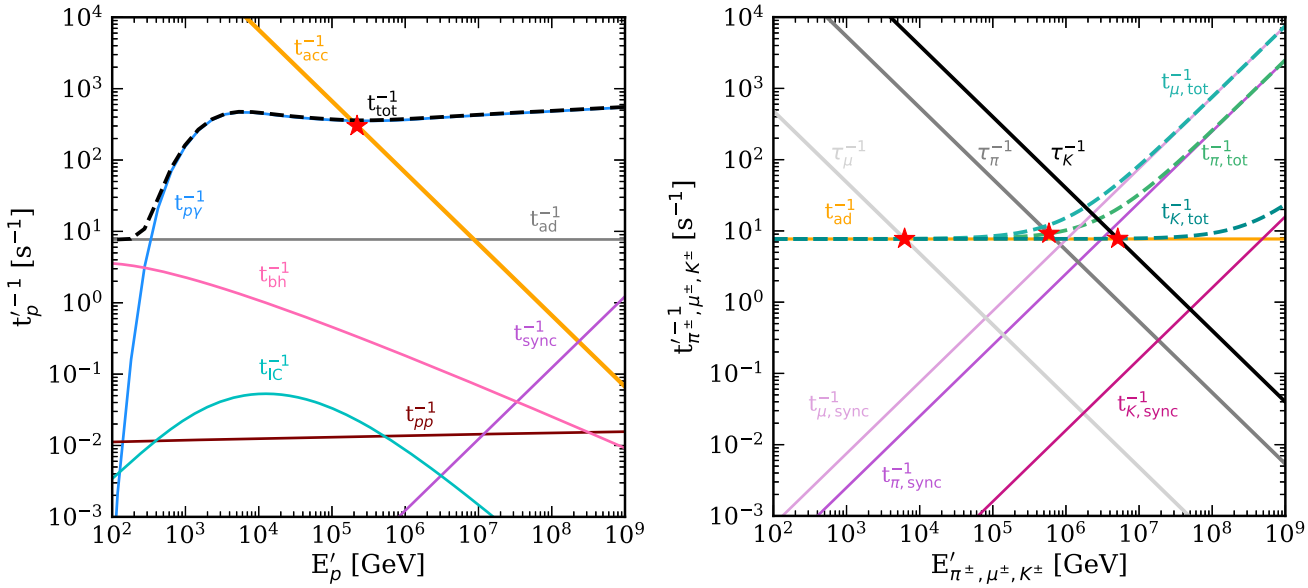

Figure 8. Cooling times of protons accelerated (left panel) and charged mesons (right panel) in the internal shock scenario as functions of the particle energy. Results are shown for $\tilde{L}_{iso} = 5 \times 10^{49}$ erg s^{-1}, $\tilde{t}_j = 20$ s, and $\Gamma = 100$. The total cooling time is plotted with a dashed black line. For protons, $p\gamma$ interactions are the most efficient energy loss mechanism, and they define the maximum energy of accelerated protons, marked with a red star. For mesons, adiabatic losses are the only relevant energy loss mechanism. The maximum energy that mesons can achieve before decaying is marked by a red star.

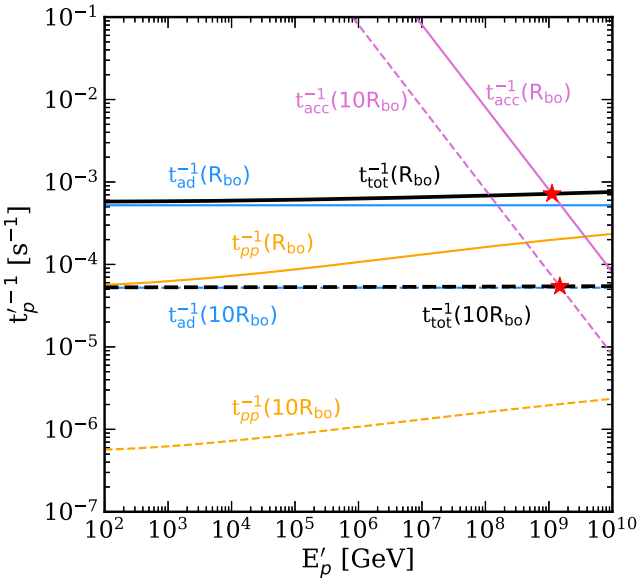

Figure 9. Cooling times of protons accelerated at the forward shock between the fast ejecta and the CSM as functions of the proton energy. We show the results at R_{bo} and $10 \times R_{bo}$ for $v_{ej} = 0.55c$, $M_{ej} = 3.7 \times 10^{-2} M_\odot$, and $M_{CSM} = 10^{-1} M_\odot$. Adiabatic cooling is the most important energy loss mechanism, while *pp* interactions are more competitive at the beginning of the evolution of the ejecta, but they rapidly drop. The red star marks the maximum energy that protons can reach in the shocked plasma shell.

more efficient at earlier times; though they are less important than adiabatic losses throughout the ejecta evolution, as expected because of the low densities of the CSM.

ORCID iDs

Ersilia Guarini https://orcid.org/0000-0002-3744-8592
Irene Tamborra https://orcid.org/0000-0001-7449-104X
Raffaella Margutti https://orcid.org/0000-0003-4768-7586

References

A. J., N., & Chandra, P. 2021, ApJL, 912, L9
Aartsen, M. G., Ackermann, M., Adams, J., et al. 2014, ApJ, 796, 109
Aartsen, M. G., Abraham, K., Ackermann, M., et al. 2017, ApJ, 835, 151
Aartsen, M. G., Ackermann, M., Adams, J., et al. 2018a, Sci, 361, eaat1378
Aartsen, M. G., Ackermann, M., Adams, J., et al. 2018b, PhRvD, 98, 062003
Aartsen, M. G., Abbasi, R., Ackermann, M., et al. 2021, JPhG, 48, 060501
Abbasi, R., Ackermann, M., Adams, J., et al. 2021a, ApJ, 910, 4
Abbasi, R., Ackermann, M., Adams, J., et al. 2021b, arXiv:2101.09836
Abbasi, R., Ackermann, M., Adams, J., et al. 2021c, PhRvD, 104, 022002
Acciari, V. A., Ansoldi, S., Antonelli, L. A., et al. 2021, ICRC (Berlin), 395, 960
Aghanim, N., Akrami, Y., Ashdown, M., et al. 2020, A&A, 641, A6
Aguilar, J. A., Allison, P., Beatty, J. J., et al. 2021, JINST, 16, P03025
Ahlers, M., & Halzen, F. 2018, PrPNP, 102, 73
Álvarez-Muñiz, J., Batista, R. A., Balagopal V., A., et al. 2020, SCPMA, 63, 219501
Anchordoqui, L. A., Barger, V., Cholis, I., et al. 2014, JHEAp, 1-2, 1
Ando, S., & Beacom, J. F. 2005, PhRvL, 95, 061103
Arcavi, I., Wolf, W. M., Howell, D. A., et al. 2016, ApJ, 819, 35
Asano, K., & Nagataki, S. 2006, ApJL, 640, L9
Baerwald, P., Hummer, S., & Winter, W. 2012, APh, 35, 508
Bietenholz, M. F., Margutti, R., Coppejans, D., et al. 2020, MNRAS, 491, 4735
Blandford, R. D., & McKee, C. F. 1976, PhFl, 19, 1130
Blaufuss, E. 2018, ATel, 11785, 1
Bright, J. S., Margutti, R., Matthews, D., et al. 2022, ApJ, 926, 112
Bromberg, O., Nakar, E., Piran, T., & Sari, R. 2011, ApJ, 740, 100
Calderón, D., Pejcha, O., & Duffell, P. C. 2021, MNRAS, 507, 1092
Caprioli, D., & Spitkovsky, A. 2014, ApJ, 783, 91
Cardillo, M., Amato, E., & Blasi, P. 2015, APh, 69, 1
Chen, C., & Shen, R.-F. 2022, RAA, 22, 035017
Coppejans, D. L., Margutti, R., Terreran, G., et al. 2020, ApJL, 895, L23
Coughlin, E. R. 2019, ApJ, 880, 108
Dai, L., & Fang, K. 2017, MNRAS, 469, 1354
Daigne, F., & Mochkovitch, R. 1998, MNRAS, 296, 275
Denton, P. B., & Tamborra, I. 2018, ApJ, 855, 37
Dermer, C. D., & Menon, G. 2009, High Energy Radiation from Black Holes: Gamma Rays, Cosmic Rays, and Neutrinos (Princeton, NJ: Princeton Univ. Press)
Drout, M. R., Chornock, R., Soderberg, A. M., et al. 2014, ApJ, 794, 23
Ellison, D. C., Patnaude, D. J., Slane, P., Blasi, P., & Gabici, S. 2007, ApJ, 661, 879
Esteban, I., Gonzalez-Garcia, M. C., Maltoni, M., Schwetz, T., & Zhou, A. 2020, JHEP, 09, 178

Fang, K., Kotera, K., Murase, K., & Olinto, A. V. 2014, PhRvD, 90, 103005
Fang, K., & Metzger, B. D. 2017, ApJ, 849, 153
Fang, K., Metzger, B. D., Murase, K., Bartos, I., & Kotera, K. 2019, ApJ, 878, 34
Fang, K., Metzger, B. D., Vurm, I., Aydi, E., & Chomiuk, L. 2020, ApJ, 904, 4
Farzan, Y., & Smirnov, A. Y. 2008, NuPhB, 805, 356
Fasano, M., Celli, S., Guetta, D., et al. 2021, JCAP, 09, 044
Finke, J. D., & Dermer, C. D. 2012, ApJ, 751, 65
Fox, O. D., & Smith, N. 2019, MNRAS, 488, 3772
Franckowiak, A., Garrappa, S., Paliya, V., et al. 2020, ApJ, 893, 162
Gaisser, T. K. 2019, arXiv:1910.08851
Gaisser, T. K., & Honda, M. 2002, ARNPS, 52, 153
Gao, S., Asano, K., & Mészáros, P. 2012, JCAP, 11, 058
Garrappa, S., Buson, S., Franckowiak, A., et al. 2019, ApJ, 880, 103
Gilkis, A., & Arcavi, I. 2022, MNRAS, 511, 691
Giommi, P., Padovani, P., Oikonomou, F., et al. 2020, A&A, 640, L4
Gottlieb, O., & Globus, N. 2021, ApJL, 915, L4
Gottlieb, O., Lalakos, A., Bromberg, O., Liska, M., & Tchekhovskoy, A. 2022a, MNRAS, 510, 4962
Gottlieb, O., Tchekhovskoy, A., & Margutti, R. 2022b, MNRAS, 513, 3810
Granot, J. 2007, RMxAA, 27, 140
Grichener, A., & Soker, N. 2021, MNRAS, 507, 1651
Guetta, D., Spada, M., & Waxman, E. 2001, ApJ, 557, 399
Guo, F., Li, H., Daughton, W., & Liu, Y.-H. 2014, PhRvL, 113, 155005
Harrison, R., Gottlieb, O., & Nakar, E. 2018, MNRAS, 477, 2128
He, H.-N., Kusenko, A., Nagataki, S., Fan, Y.-Z., & Wei, D.-M. 2018, ApJ, 856, 119
He, H.-N., Liu, R.-Y., & Wang, X.-Y. 2012, ApJ, 752, 29
Ho, A. Y. Q., Phinney, S. E., Ravi, V., et al. 2019, ApJ, 871, 73
Ho, A. Y. Q., Perley, D. A., Kulkarni, S. R., et al. 2020, ApJ, 895, 49
Ho, A. Y. Q., Perley, D. A., Gal-Yam, A., et al. 2021, arXiv:2105.08811
Hummer, S., Ruger, M., Spanier, F., & Winter, W. 2010, ApJ, 721, 630
Inserra, C. 2019, NatAs, 3, 697
Jones, F. C. 1965, PhRv, 137, B1306
Kadler, M., Krauß, F., Mannheim, K., et al. 2016, NatPh, 12, 807
Kashiyama, K., Murase, K., Horiuchi, S., Gao, S., & Meszaros, P. 2013, ApJL, 769, L6
Kashiyama, K., & Quataert, E. 2015, MNRAS, 451, 2656
Katz, B., Sapir, N., & Waxman, E. 2011, arXiv:1106.1898
Kelner, S. R., Aharonian, F. A., & Bugayov, V. V. 2006, PhRvD, 74, 034018
Kilian, P., Li, X., Guo, F., & Li, H. 2020, ApJ, 899, 151
Kippenhahn, R., Weigert, A., & Weiss, A. 1990, Stellar Structure and Evolution, Vol. 192 (Berlin: Springer)
Kobayashi, S., Piran, T., & Sari, R. 1997, ApJ, 490, 92
Krauß, F., Deoskar, K., Baxter, C., et al. 2018, A&A, 620, A174
Kuin, N. P. M., Wu, K., Oates, S., et al. 2019, MNRAS, 487, 2505
Kumar, P., & Zhang, B. 2014, PhR, 561, 1
Leung, S.-C., Blinnikov, S., Nomoto, K., et al. 2020, ApJ, 903, 66
Levinson, A., & Bromberg, O. 2008, PhRvL, 100, 131101
Lipari, P., Lusignoli, M., & Meloni, D. 2007, PhRvD, 75, 123005
Liu, L.-D., Zhang, B., Wang, L.-J., & Dai, Z.-G. 2018, ApJL, 868, L24
Lunardini, C., & Winter, W. 2016, PhRvD, 95, 123001
Lyutikov, M. 2022, MNRAS, 515, 2293
Lyutikov, M., & Toonen, S. 2019, MNRAS, 487, 5618
Malkov, M. A., & Drury, L. O. 2001, RPPh, 64, 429
Margalit, B., & Quataert, E. 2021, ApJL, 923, L14
Margutti, R., Metzger, B., Chornock, R., et al. 2019, ApJ, 872, 18
Matthews, J., Bell, A., & Blundell, K. 2020, NewAR, 89, 101543
Matzner, C. D., & McKee, C. F. 1999, ApJ, 510, 379
Mészáros, P. 2017a, ARNPS, 67, 45
Mészáros, P. 2017b, in Neutrino Astronomy, ed. T. Gaisser & A. Karle (Singapore: World Scientific), 1
Meszaros, P., & Rees, M. J. 2001, ApJL, 556, L37
Meszaros, P., & Waxman, E. 2001, PhRvL, 87, 171102
Metzger, B. D. 2022, ApJ, 932, 84
Metzger, B. D., Giannios, D., Thompson, T. A., Bucciantini, N., & Quataert, E. 2011, MNRAS, 413, 2031
Mizuta, A., & Ioka, K. 2013, ApJ, 777, 162
Modjaz, M., Gutierrez, C. P., & Arcavi, I. 2019, NatAs, 3, 717
Murase, K. 2017, in Neutrino Astronomy, ed. T. Gaisser & A. Karle (Singapore: World Scientific), 15
Murase, K., & Bartos, I. 2019, ARNPS, 69, 477
Murase, K., & Ioka, K. 2013, PhRvL, 111, 121102
Murase, K., Kimura, S. S., Zhang, B. T., Oikonomou, F., & Petropoulou, M. 2020, ApJ, 902, 108
Murase, K., Meszaros, P., & Zhang, B. 2009, PhRvD, 79, 103001
Murase, K., Thompson, T. A., Lacki, B. C., & Beacom, J. F. 2011, PhRvD, 84, 043003
Murase, K., Thompson, T. A., & Ofek, E. O. 2014, MNRAS, 440, 2528
Nakar, E. 2015, ApJ, 807, 172
Nalewajko, K., Uzdensky, D. A., Cerutti, B., Werner, G. R., & Begelman, M. C. 2015, ApJ, 815, 101
Necker, J., de Jaeger, T., Stein, R., et al. 2022, arXiv:2204.00500
Olinto, A. V., Krizmanic, J., Adams, J. H., et al. 2021, JCAP, 06, 007
Ostriker, J. P., & Gunn, J. E. 1969, ApJ, 157, 1395
Particle Data Group, Zyla, P. A., Barnett, R. M., et al. 2020, PTEP, 2020, 083C01
Pasham, D. R., Ho, W. C. G., Alston, W., et al. 2022, NatAs, 6, 249
Patnaude, D. J., & Fesen, R. A. 2009, ApJ, 697, 535
Pellegrino, C., Howell, D. A., Vinko´, J., et al. 2022, ApJ, 926, 125
Perley, D. A., Mazzali, P. A., Yan, L., et al. 2019, MNRAS, 484, 1031
Petropoulou, M., Coenders, S., Vasilopoulos, G., Kamble, A., & Sironi, L. 2017, MNRAS, 470, 1881
Petropoulou, M., Giannios, D., & Dimitrakoudis, S. 2014, MNRAS, 445, 570
Petropoulou, M., Kamble, A., & Sironi, L. 2016, MNRAS, 460, 44
Petropoulou, M., & Sironi, L. 2018, MNRAS, 481, 5687
Piro, A. L., & Lu, W. 2020, ApJ, 894, 2
Pitik, T., Tamborra, I., Angus, C. R., & Auchettl, K. 2022, ApJ, 929, 163
Pitik, T., Tamborra, I., & Petropoulou, M. 2021, JCAP, 05, 034
Poznanski, D., Chornock, R., Nugent, P. E., et al. 2010, Sci, 327, 58
Prentice, S. J., Maguire, K., Smartt, S. J., et al. 2018, ApJL, 865, L3
Protheroe, R. J., & Clay, R. W. 2004, PASA, 21, 1
Pursiainen, M., Childress, M., Smith, M., et al. 2018, MNRAS, 481, 894
Quataert, E., Lecoanet, D., & Coughlin, E. R. 2019, MNRAS, 485, L83
Razzaque, S., Meszaros, P., & Waxman, E. 2004, PhRvL, 93, 181101
Razzaque, S., Mészáros, P., & Waxman, E. 2005, MPLA, 20, 2351
Razzaque, S., & Yang, L. 2015, PhRvD, 91, 043003
Reusch, S., Stein, R., Kowalski, M., et al. 2022, PhRvL, 128, 221101
Sari, R., & Piran, T. 1995, ApJL, 455, L143
Sarmah, P., Chakraborty, S., Tamborra, I., & Auchettl, K. 2022, JCAP, 2022, 011
Sato, T., Katsuda, S., Morii, M., et al. 2018, ApJ, 853, 46
Schure, K. M., Achterberg, A., Keppens, R., & Vink, J. 2010, MNRAS, 406, 2633
Senno, N., Murase, K., & Meszaros, P. 2016, PhRvD, 93, 083003
Senno, N., Murase, K., & Mészáros, P. 2017, ApJ, 838, 3
Sironi, L., & Spitkovsky, A. 2011, ApJ, 726, 75
Sironi, L., Spitkovsky, A., & Arons, J. 2013, ApJ, 771, 54
Slane, P., Lee, S. H., Ellison, D. C., et al. 2014, ApJ, 783, 33
Sobacchi, E., Granot, J., Bromberg, O., & Sormani, M. C. 2017, MNRAS, 472, 616
Soker, N. 2022, RAA, 22, 055010
Soker, N., Grichener, A., & Gilkis, A. 2019, MNRAS, 484, 4972
Stanev, T. 2010, High Energy Cosmic Rays (Berlin: Springer)
Stein, R. 2021, ICRC (Madison, WI), 358, 1016
Stein, R., van Velzen, Sjoert, Kowalski, M., et al. 2021, NatAs, 5, 510
Stein, R., Reush, S., Franckowiak, A., et al. 2022, arXiv:2203.17135
Strotjohann, N. L., Kowalski, M., & Franckowiak, A. 2019, A&A, 622, L9
Sturner, S. J., Skibo, J. G., Dermer, C. D., & Mattox, J. R. 1997, ApJ, 490, 619
Sun, N.-C., Maund, J. R., Crowther, P. A., & Liu, L.-D. 2022, MNRAS, 512, L66
Suzuki, A., Moriya, T. J., & Takiwaki, T. 2020, ApJ, 899, 56
Tamborra, I., & Ando, S. 2015, JCAP, 09, 036
Tamborra, I., & Ando, S. 2016, PhRvD, 93, 053010
Tamborra, I., Ando, S., & Murase, K. 2014, JCAP, 09, 043
Tan, J. C., Matzner, C. D., & McKee, C. F. 2001, ApJ, 551, 946
Tanaka, M., Tominaga, N., Morokuma, T., et al. 2016, ApJ, 819, 5
Uno, K., & Maeda, K. 2020, ApJ, 897, 156
Vallely, P. J., Kochanek, C. S., Stanek, K. Z., Fausnaugh, M., & Shappee, B. J. 2020, MNRAS, 500, 5639
Vitagliano, E., Tamborra, I., & Raffelt, G. 2020, RvMP, 92, 45006
Wang, X.-Y., & Liu, R.-Y. 2016, PhRvD, 93, 083005
Waxman, E. 2017, in Neutrino Astronomy, ed. T. Gaisser & A. Karle (Singapore: World Scientific), 33
Xiang, D., Wang, X., Lin, W., et al. 2021, ApJ, 910, 42
Xiao, D., & Dai, Z. G. 2014, ApJ, 790, 59
Yao, Y., Ho, A. Y. Q., Medvedev, P., et al. 2022, ApJ, 934, 104
Yuksel, H., Kistler, M. D., Beacom, J. F., & Hopkins, A. M. 2008, ApJL, 683, L5
Zandanel, F., Tamborra, I., Gabici, S., & Ando, S. 2015, A&A, 578, A32
Zhang, B. T., & Murase, K. 2019, PhRvD, 100, 103004
Zirakashvili, V. N., & Ptuskin, V. S. 2016, APh, 78, 28
Zyla, P. A., Barnett, R. M., Beringer, J., et al. 2020, PTEP, 2020, 083C01